

GIERING, S.L.C., CARVALHO, F., IVERSEN, M.H., LIU, Z., MERCHERS, O., MOORE, C.M., OCKWELL, M., PASSOW, U., POULTON, A.J., ROMANELLI, E., THEVAR, T. and SANDERS, R. 2025. Species-specific diatom dynamics shape their vertical distribution and export during bloom decline. *Limnology and oceanography* [online], 70(4), pages 959-976.
Available from: <https://doi.org/10.1002/lno.12818>

Species-specific diatom dynamics shape their vertical distribution and export during bloom decline.

GIERING, S.L.C., CARVALHO, F., IVERSEN, M.H., LIU, Z., MERCHERS, O., MOORE, C.M., OCKWELL, M., PASSOW, U., POULTON, A.J., ROMANELLI, E., THEVAR, T. and SANDERS, R.

2025

© 2025 The Author(s). *Limnology and Oceanography* published by Wiley Periodicals LLC on behalf of Association for the Sciences of Limnology and Oceanography.
Supplementary materials are appended after the main text of this document.

RESEARCH ARTICLE

Species-specific diatom dynamics shape their vertical distribution and export during bloom decline

Sarah L. C. Giering ^{1*}, Filipa Carvalho ¹, Morten H. Iversen ^{2,3}, Zonghua Liu,^{1,4} Océane Merchiers ⁵,
C. Mark Moore,⁵ Michael Ockwell,⁶ Uta Passow ⁷, Alex J. Poulton ⁸, Elisa Romanelli,⁹
Thangavel Thevar,¹⁰ Richard Sanders^{11,12}

¹National Oceanography Centre, Southampton, UK; ²Alfred Wegener Institute Helmholtz-Center for Polar and Marine Research Bremerhaven, Bremerhaven, Germany; ³MARUM and University of Bremen, Bremen, Germany; ⁴School of Computing, Engineering and Technology, Robert Gordon University, Aberdeen, UK; ⁵School of Ocean and Earth Science, National Oceanography Centre Southampton, University of Southampton, Southampton, UK; ⁶Hi-Z 3D Ltd, London, UK; ⁷Memorial University, St John's, Newfoundland and Labrador, Canada; ⁸The Lyell Centre for Earth and Marine Sciences, Heriot-Watt University, Edinburgh, UK; ⁹Earth Research Institute, University of California, Santa Barbara, California, USA; ¹⁰School of Engineering, University of Aberdeen, Aberdeen, UK; ¹¹Norwegian Research Centre, Bergen, Norway; ¹²Bjerkenes Centre for Climate Research, Bergen, Norway

Abstract

The Southern Ocean is a critical region for global biogeochemical cycles, particularly for carbon dioxide uptake and organic carbon export, partly driven by extensive phytoplankton blooms. In naturally iron-fertilized regions of this otherwise iron-limited ocean, these blooms are primarily driven by diatoms. Variability in bloom occurrences on spatiotemporal scales makes it challenging to track and understand a bloom's decline and associated carbon export. Moreover, species-specific processes may be critical yet are typically not well resolved. Here, we use state-of-the-art in situ imaging, producing high-resolution vertical profiles of phytoplankton and particles, combined with water sampling, to resolve the decline of a Southern Ocean spring bloom. We observed significant vertical and temporal changes in particle and diatom composition and abundance. *Fragilariopsis kerguelensis* showed deepening abundance peaks correlating with silicic acid gradients and water density changes, while their chain lengths decreased likely due to nutrient stress and physical breakage. High downward fluxes of *F. kerguelensis* and concentrations below the mixed layer suggest they were a key contributor to carbon export and transfer. Conversely, *Eucampia antarctica* exhibited a rapid decline in surface abundance with minimal vertical redistribution and low fluxes, potentially linked to changing environmental conditions. These findings highlight species-specific responses to environmental conditions and implications for carbon processes. Measured values of the apparent photosynthetic efficiency (Fv/Fm) suggests that photosynthetically viable diatoms were a significant contributor to export and particle biomass in the upper mesopelagic zone. Our results underscore the importance of understanding individual species dynamics for oceanic carbon and nutrient cycles.

*Correspondence: s.giering@noc.ac.uk

This is an open access article under the terms of the [Creative Commons Attribution](https://creativecommons.org/licenses/by/4.0/) License, which permits use, distribution and reproduction in any medium, provided the original work is properly cited.

Associate editor: Katherina Petrou

Data Availability Statement: Data are available from the lead author on request. CTD data are available from <https://doi.org/10.1594/PANGAEA.963390>.

The Southern Ocean is a key player in global biogeochemical cycles, accounting for up to 50% of annual oceanic CO₂ uptake, in part due to the large annual phytoplankton bloom that contributes ~30% to global organic carbon export (Schlitzer 2002; Gruber, Landschützer, and Lovenduski 2019). The Southern Ocean spring bloom is one of the largest phytoplankton blooms in the world, covering vast areas of the ocean's surface. It provides a seasonal food source for zooplankton, fish, seabirds, and marine mammals, supporting the entire Southern

Ocean ecosystem. Spring blooms in naturally iron-fertilized regions of the otherwise iron-limited Southern Ocean are primarily driven by diatoms (Blain et al. 2007; Korb et al. 2008) that typically rapidly explode in numbers once light availability increases (Soppa, Völker, and Bracher 2016). These blooms are thought to terminate due to a combination of factors, including nutrient depletion (Smetacek 1999; Smetacek, Assmy, and Henjes 2004) and changes in light availability (de Baar 2005; Moore et al. 2007). Around the naturally iron-fertilized region of South Georgia, predicted to be the strongest carbon sink in the Southern Ocean (Schlitzer 2002), silicate and iron depletion are thought to be the key limiting factors (Nielsdóttir et al. 2012; Borriore and Schlitzer 2013; Ainsworth et al. 2023). Grazing pressure by large zooplankton and other higher trophic levels has also been suggested to control the diatom community biomass and composition as well as contributing to bloom dynamics (Smetacek, Assmy, and Henjes 2004).

The ultimate fate of phytoplankton, including diatoms, toward the end of a bloom varies depending on environmental conditions and biological processes. As nutrient supply becomes depleted, phytoplankton cells can undergo senescence, a natural process of aging and deterioration. Some species form resting spores following nutrient depletion (Kuwata, Hama, and Takahashi 1993; Peters and Thomas 1996). Senescent cells and resting spores may sink out of the surface ocean to deeper waters or the seafloor (Salter et al. 2012; Rembauville et al. 2015). Another process that leads to the vertical loss of phytoplankton biomass is aggregation of cells into “marine snow” (Alldredge and Silver 1988; Thornton 2002; Burd and Jackson 2009). Marine snow can sink rapidly through the water column, transporting organic matter to depth. Aggregation via collision may result from viral (e.g., Yamada et al. 2018; Kranzler et al. 2019) and parasitic infections of phytoplankton (e.g., Kagami et al. 2007; Klawonn et al. 2023). Finally, grazing by zooplankton and other higher trophic levels contributes to the transfer of carbon and nutrients up the food chain. Some of the ingested material will be repackaged into sinking fecal matter that also contributes to the downward transport of organic matter (e.g., Manno et al. 2015, 2022), while the remaining matter is converted into biomass, respired or excreted (e.g., Ikeda 1985; Steinberg, Silver, and Pilskaln 1997; Giering et al. 2012).

A challenge in tracking and understanding the fate of phytoplankton during a bloom’s decline is the variability in the occurrence of blooms on horizontal, vertical and temporal scales. Traditional oceanographic survey methods frequently fail to detect these sporadic events or underestimate their importance for the export of carbon to depth (Buesseler 1998). Moreover, species-specific processes may not be resolved. The importance of species-focused approaches is now increasingly recognized, especially concerning the impact of diatoms on export processes (Twining, Baines, and Fisher 2004; Kemp et al. 2006; Tréguer et al. 2018). To better understand biogeochemical processes that underpin the modeling of oceanic carbon and nutrient cycles,

the identification of key species and functional groups and their interaction within the ecosystem is critical (Kemp et al. 2006; Tréguer et al. 2018; Lafond et al. 2020).

In this study, we focus on two diatom species: *Fragilariopsis kerguelensis* and *Eucampia antarctica*. *F. kerguelensis* is a heavily silicified diatom species which can dominate the ice-free, off-shore Antarctic Circumpolar Current (Smetacek, Assmy, and Henjes 2004). Identifiable by its ribbon-shaped chains and robust frustules, *F. kerguelensis* exhibits high mechanical resistance to grazing (Hamm et al. 2003). Its prevalence contributes significantly to the sedimentary Antarctic opal belt, the world’s largest biogenic silica deposit, making it a key player in the global silicon cycle (Tréguer et al. 1995; Zielinski and Gersonde 1997). Moreover, *F. kerguelensis* has been demonstrated to be adapted to thrive in iron-limited waters (Timmermans and Van Der Wagt 2010; Strzepek et al. 2011), readily responding to iron addition (Boyd et al. 2000; Blain et al. 2007; Hoffmann, Peeken, and Lochte 2007), and can dominate export (e.g., Rigual-Hernández et al. 2015).

Eucampia antarctica var *antarctica* is a silicified diatom that is found in the warmer waters of the Polar Front Zone and Subantarctic Zone and is identifiable by its long spiral chains (Fryxell 1991; Allen 2014). Elevated abundances, even dominating blooms, have been reported near islands including Crozet (Poulton et al. 2007; Salter et al. 2007), Kerguelen (Fryxell 1991; Armand et al. 2008) and South Georgia (Froneman, Pakhomov, and Laubscher 1997; Ward et al. 2007; Korb et al. 2008). This species is only moderately abundant in surface sediments of the Southern Ocean (Allen 2014), with variable relative flux rates (at 87–128 m depth) ranging from 0% to 98% contribution to total cell counts in sinking material (Salter et al. 2007). Its ecology and spatial distribution are unclear but may be linked to coastal conditions, melting ice and associated melt-water-induced buoyancy, and nutrient (iron) availability (Armand et al. 2008; Salter et al. 2012), possibly owing to its enhanced ability to grow at low silicic acid concentrations (Armand et al. 2008; Mosseri et al. 2008).

We here use state-of-the-art in situ imaging, producing high-resolution vertical profiles of phytoplankton and particles, combined with in situ sampling, including Marine Snow Catchers (MSCs), to resolve the decline of a Southern Ocean spring bloom for individual diatom species. Specifically, we follow the decline of the diatom spring bloom at the naturally iron-fertilized, long-term monitoring site P3 near South Georgia and discuss the likely fate of *F. kerguelensis* and *E. antarctica* during the bloom’s decline. This work is part of the Controls over Ocean Mesopelagic Interior Carbon Storage (COMICS) program, whose focus is to unravel the controls of downward carbon transport (Sanders et al. 2016).

Materials and methods

Field campaign

Vertical profiles of plankton and particles were captured using the LISST-Holo (Sequoia, US) and the MSC within the

framework of the UK COMICS program (Controls over Ocean Mesopelagic Interior Carbon Storage; Sanders et al. 2016). The expedition focused on examining the diatom bloom in a highly productive area downstream of South Georgia during Nov/Dec 2017 (cruise DY086). We visited the naturally iron-fertilized, long-term monitoring site “P3” (52.4°S, 40.1°W; Fig. 1a; Manno et al. 2015) three times over a period of 4.5 weeks, with each visit lasting ~7 d: 15 Nov to 22 Nov (P3A), 29 Nov to 5 Dec (P3B), and 9 Dec to 15 Dec 2017 (P3C). In addition, we sampled near the site “P2” upstream of South Georgia (~56.5°S 41.0°W), which is more iron-deficient and has low productivity levels (Korb et al. 2008; Nielsdóttir et al. 2012; Borrione and Schlitzer 2013). We include P2 as “reference station” for non-bloom conditions and as it shows a radically different particle composition, but as it was under-sampled compared to P3 we do not discuss it further.

Our analysis encompasses data from a total of 11 LISST-Holo profiles and 10 MSC profiles (made up of a total of 42 individual MSC deployments) (Supporting Information Table S1). In addition, water column properties (temperature, salinity, potential water density anomaly, chlorophyll fluorescence, nitrate, phosphate, silicate, dissolved iron, and chlorophyll-*a*) were measured from a total of 33 Niskin rosette casts (25 of which were made using a stainless steel frame) fitted with conductivity, temperature and depth units (SBE 911plus/917plus). Analytical details are described in the Supporting Information.

Hologram collection, extraction, and sizing

The LISST-Holo (Graham and Nimmo Smith 2010) was fitted to the “Red Camera Frame”, a modified lander platform, and operated with an external battery pack. For each profile, the Red Camera Frame was submerged to ~230 m, capturing a holographic image with a volume of 1.86 cm³ at intervals of 1.2–2.5 m. Detailed methods are described in the Supporting Information. Briefly, the holograms were processed using FastScan (Thevar et al. 2023) including hologram reconstruction, particle autofocus and extraction. The pixel size of the extracted image (“vignette”) was 4.4 μm. Particle size was extracted from these vignettes using the machine-learning-based method developed by Liu et al. (2023). Note that the volume for delicate particles with enclosed empty space may be overestimated (*see* Supporting Information), though these particles were rare. Equivalent spherical diameter (in mm) of a particle was calculated from the area (*A* in pixel) of the particle.

Particle details calculated from the holograms were then summarized in 5-m depth bins. For the depth profiles, only holograms from a depth of ≥5 m were used to avoid introducing artifacts from sampling near the surface (i.e., higher chance of encountering bubbles, schlieren, light pollution).

Sinking material—Marine Snow Catcher and FlowCam

Sinking particle profiles were obtained using the MSC (Fig. 1b). Detailed methods are described in the Supporting

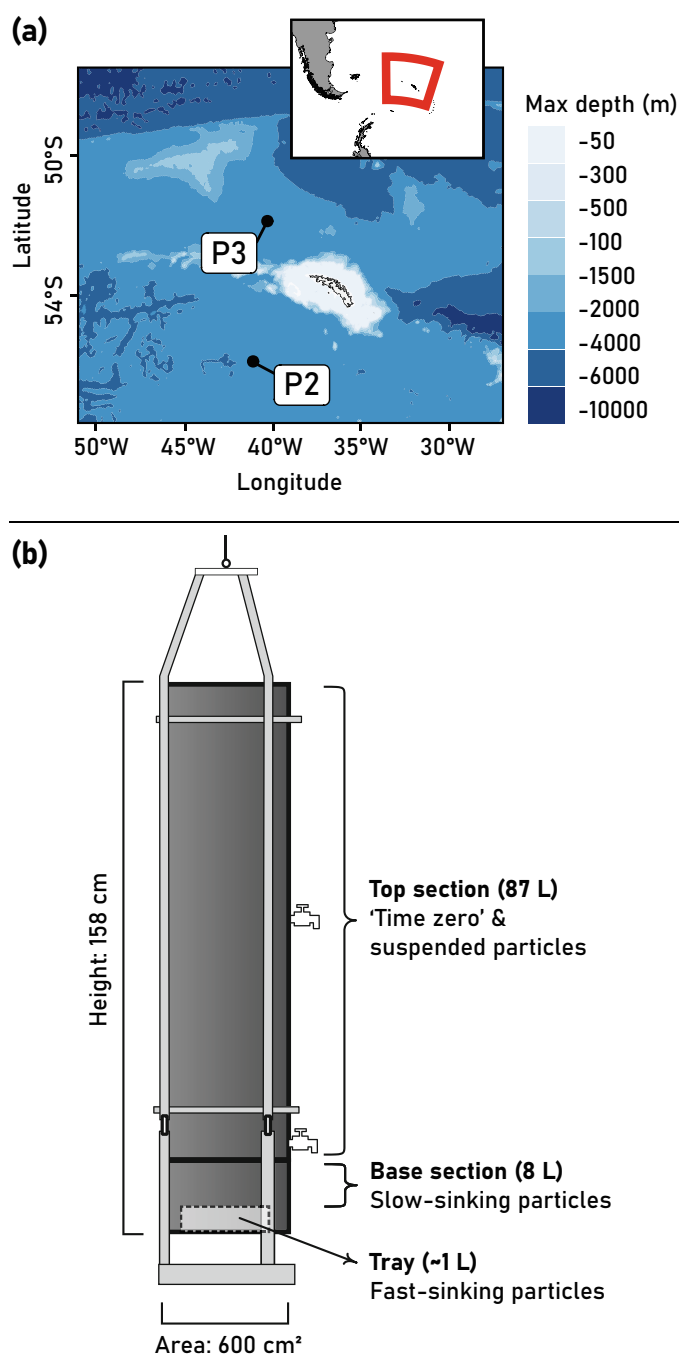


Fig. 1. (a) Study sites P3 (52.4°S, 40.1°W) and P2 (56.5°S 41.0°W) in the vicinity of South Georgia. Map adapted with permission from Giering et al. (2023). (b) Schematic of Marine Snow Catcher. Adapted with permission from Giering et al. (2016).

Information and, including results, by Giering et al. (2023). Briefly, the MSC is a large sampling bottle (95 L capacity) deployed open to specific depths (50–500 m) and equipped with a removable base section (8 L) containing a tray (~1 L). After recovery, a 5-L “time zero” sample (T_0) was taken from the top section, followed by a 2-h settling period on deck to

separate suspended and fast-sinking particles (FSP), which were collected by the tray. Concentrations and fluxes of chlorophyll-*a*, biogenic silica, and particulate organic carbon for each fraction are presented by Giering et al. (2023) and Williams et al. (2024). Here, we analyzed the taxonomic microplankton community composition of the T_0 and Tray samples. Subsamples (50–200 mL) were preserved with 3.6% formaldehyde (buffered with di-sodium tetraborate). No formaldehyde samples were taken at P3C.

To identify and quantify particles collected by the MSC, we processed 10 mL of each formaldehyde-preserved sample using FlowCam 8410 (Yokogawa Fluid Imaging Technologies Inc.). Detailed methods are described by Romanelli et al. (2023). Image pixel size was 1.4 μm , and we identified only objects larger than $\sim 80 \mu\text{m}$ in diameter. Images were classified manually using the EcoTaxa platform (Picheral, Colin, and Irisson 2017). Using Python, images were converted to greyscale (where 0 means black and 255 means white) and a threshold value of 160 was applied to determine particle regions (see Supporting Information). Equivalent spherical diameter and volume were calculated using the same equations applied to the hologram vignettes.

The numerical concentration of sinking cells (C_{sink} in n mL^{-1}) and resulting fluxes (F in $\text{n cm}^{-2} \text{d}^{-1}$) of *F. kerguelensis* and *E. antarctica* were calculated based on the equations by Giering et al. (2016, 2023) with slight modifications (see Supporting Information). The percentage of sinking cells was calculated as the ratio between C_{sink} and the concentrations in the T_0 samples (C_{T_0}).

Taxonomic classification

Particle classification was carried out on the EcoTaxa platform. All images were manually verified by at least two different experts from the author list. Images were assigned to 36 classes (Table 1) in seven overall class groups (diatom, non-diatom phytoplankton, zooplankton, detritus, fecal matter, others, and unwanted). Images in the “unwanted” class group were removed from all analyses.

Photosynthetic efficiency

The apparent photochemical efficiency (Fv/Fm) of phytoplankton within particulate material was measured with a prototype “single turnover fluorescence of enclosed samples (STAFES)” instrument (Chelsea Technologies [UK] Ltd.) using protocols similar to those used previously (Moore et al. 2007; Nielsdóttir et al. 2012; Schuback et al. 2024). Measurements were made on discrete samples from MSC fractions and a series of dark incubation experiments detailed below. Values of Fv/Fm were all corrected for blanks measured on filtered seawater (Cullen and Davis 2003), with absolute blank values being relatively invariant with depth, but increasing from typical values of <5% of Fm to >10% within the lowest biomass samples measured.

Table 1. Taxonomic level of classification of images (based on LISST-Holo images).

Class group	Class
Diatom	<i>Chaetoceros</i> chain, <i>Chaetoceros socialis</i> , <i>Corethron</i> spp., <i>Dactyliosolen</i> , <i>Diatoma</i> spp., <i>Eucampia antarctica</i> var <i>antarctica</i> , <i>Fragilariopsis kerguelensis</i> , various pennates, <i>Rhizosolenia</i> , <i>Thalassionema</i> spp., <i>Thalassiosira</i> spp., <i>Thalassiothrix</i> spp.
Non-diatom phytoplankton	Ciliophora, dinoflagellates, tripos, long chains of unclear phytoplankton origin
Zooplankton	Appendicularia, chaetognatha, copepod, gastropod, nauplii, polychaete, radiolaria, tintinnid
Detritus	Detritus (including aggregates)
Fecal matter	Fecal pellets
Other	Cylinder, multiple, ring, round, sphere, unidentified cells, unknown of marine origin
Unwanted	Bubble, duplicate, noise

Three experiments were undertaken with water collected from either the underway sampling system (P3A) or a trace metal clean CTD (P3B & P3C) to investigate the evolution of Fv/Fm within diatom populations maintained in the dark. Samples collected within the mixed layer (≤ 30 m) were dispensed into individual acid-cleaned 50-mL plastic centrifuge tubes and incubated for between 6 and 16 d, with individual subsamples sacrificed for daily measurements.

Statistics

The hydrodynamic disturbances caused by the “Red Camera Frame” could lead to relatively higher fragmentation of particles during the upcast relative to the downcast (the instruments are fitted at the bottom of the frame to minimize turbulence during the downcast). We did not find a systematic statistical difference in downcast vs. upcast in any of the particle characteristics (see Supporting Information). We therefore included all profiles and combined downcast and upcast data when computing the depth profiles for further data analyses.

To visualize the variability in particle composition, we used non-metric multidimensional scaling (NMDS) from the vegan package in R (Oksanen et al., 2016; R Core Team, 2023) on the depth binned particle classes. Distances were calculated using Bray–Curtis dissimilarity, and the solution was centered, scaled to a half-change scale, and rotated so that the x-axis approximates depth.

Results

Hydrographic conditions

Potential water density in the upper 50 m decreased throughout the cruise from 1026.99 to 1026.93 to 1026.90 kg/m^3 for P3A, P3B and P3C, respectively, owing to a warming of the

surface temperature (from 2.36°C to 3.06°C to 3.42°C, respectively) rather than changes in salinity (Fig. 2a–c). While water density was fairly homogenous throughout the upper 50 m during P3A, with a density range of 1026.99–1027.07 kg m⁻³ between 0 and 86 m depth, the warming pushed this density layer to a narrow zone deeper in the water column (63–80 m and 69–80 m depth during P3B and P3C, respectively).

Profiles of nitrate, phosphate and silicic acid showed the typical nutrient profiles with lower concentrations in the near-surface and increasing concentrations with depth (Fig. 2d–f). In the near-surface at P3, nitrate and silicic acid concentrations decreased throughout the cruise, with silicic acid reaching near-zero concentrations whereas nitrate remained ~18–20 μM. Phosphate concentration profiles remained fairly constant throughout the cruise. Dissolved iron in the top 250 m at P3 increased throughout the cruise

(Fig. 2g; Ainsworth et al. 2023), whereas chlorophyll-*a* concentrations in the top 100 m decreased (Fig. 2h).

LISST-Holo versus Marine Snow Catcher plus FlowCam

We compare the results from two different sampling and imaging devices: images taken by the in situ profiling camera system LISST-Holo and by the ex situ bench-top flow-through camera system FlowCam (for example images see Supplementary Information Table S2). The LISST-Holo captures particles in situ, more or less undisturbed bar any turbulence caused by the camera frame, while the FlowCam imaged samples were collected by the MSC and subsequently stored in 4% formaldehyde until later analysis in the lab. The latter particles hence experienced a considerable amount of handling, which may alter their shape and color.

Depth profiles of the abundance and mean chain length of both *F. kerguelensis* and *E. antarctica* show good agreement

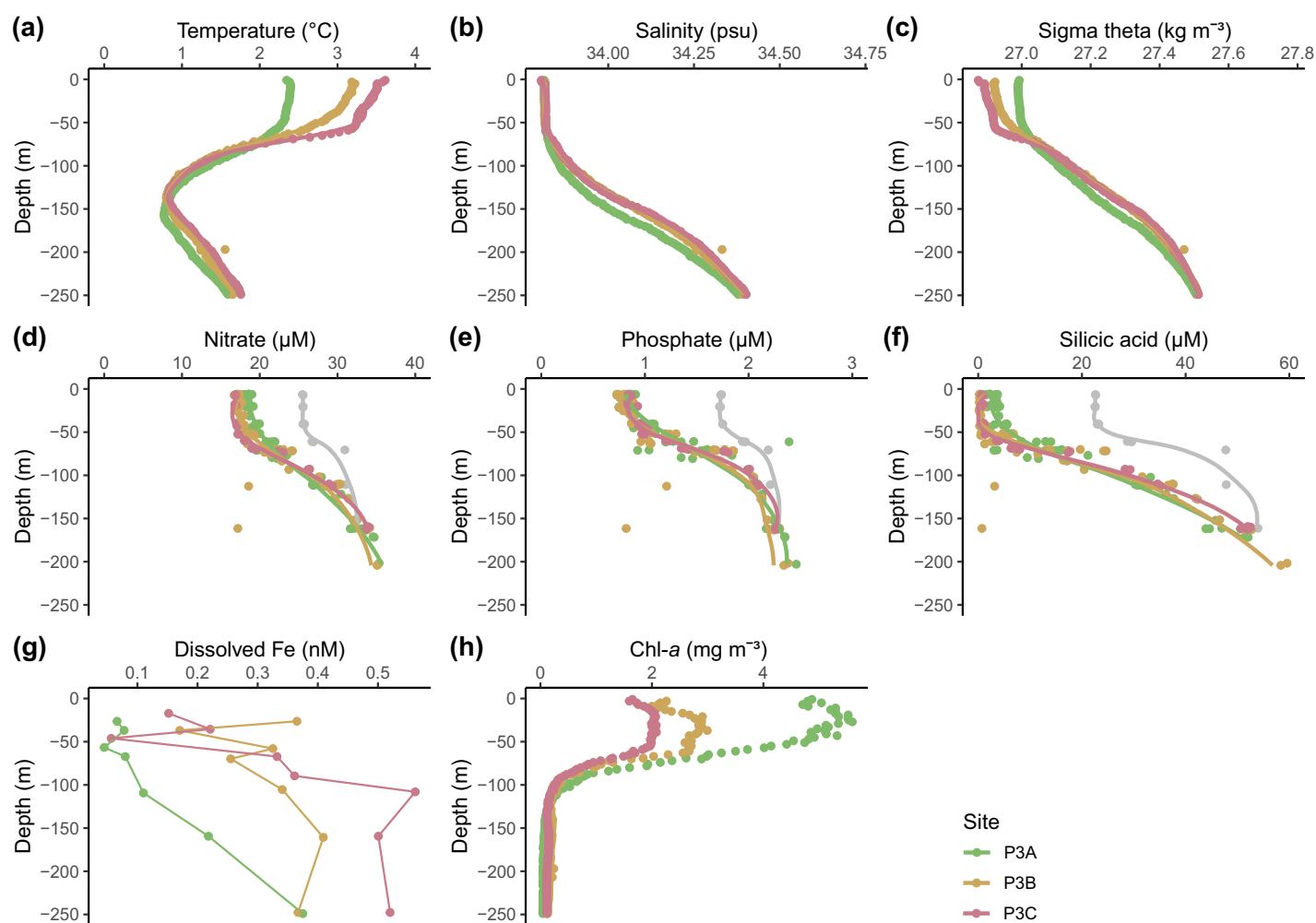


Fig. 2. Vertical profiles of environmental conditions during the study period. (a) Temperature, (b) salinity, (c) potential water density anomaly, (d) nitrate, (e) phosphate, (f) silicic acid, (g) dissolved iron (dFe), and (h) chlorophyll-*a* (Chl-*a*). Colors indicate the different visits: P2 in gray, P3A–P3C in green, orange and red, respectively. Temperature, salinity, density anomaly and Chl-*a* (based on calibrated fluorescence) are averaged in 1-m bins. For nitrate, phosphate and silicic acid, loess smoothing was applied to aid visualization. Data for dissolved iron were collected by Ainsworth et al. (2023).

between LISST-Holo and MSC + FlowCam measurements (Supporting Information Figs. S1, S2). The only noticeable divergence was the abundance of *E. antarctica* during P3A, where length estimates by LISST-Holo were approximately twice those by the MSC + FlowCam (Supporting Information Fig. S1). Relative distribution plots indicate that FlowCam seems to miss the largest chains, particularly for *E. antarctica* (Supporting Information Fig. S2), which could be a result of the more destructive sampling and preservation compared to the in situ LISST-Holo system.

Evolution of particle composition

Changes in the vertical structure of particle composition was primarily driven by diatoms, which dominated in the near-surface ocean (0–100 m) at the peak of the bloom downstream of South Georgia (P3A-B; Figs. 3, 4). The ordination plots demonstrate a clear separation between the particle composition in the near-surface ocean (0–100 m) and the upper mesopelagic zone (100–250 m) throughout all visits (Supporting Information Fig. S3). Yet, as the bloom declined, particle composition in the upper ocean became more similar to the mesopelagic

zone and the non-bloom site P2 upstream of South Georgia. The composition of particles in the upper mesopelagic zone (100–250 m) during all visits was fairly consistent, dominated by detritus and unidentifiable particles (Fig. 3).

The patterns of vertical profiles of volumetric diatom contribution were heavily influenced by diatom type, with *Thalassiothrix* and *C. socialis* dominating the volume profiles despite relatively low abundance, owing to their large size (Fig. 4). In terms of cellular abundance, *F. kerguelensis* and *E. antarctica* dominated the diatom assemblages at P3, and their individual progressions and ecological implications are discussed in detail below.

Size, abundance, and fluxes of *F. kerguelensis*, *E. antarctica*, and detritus

During P3A, we observed a high abundance of large *F. kerguelensis* chains peaking at 50–100 m depth (1.2 ± 0.3 chains mL^{-1} with a mean length of 0.18 ± 0.03 mm; Fig. 5a,b). Both the abundance and mean length of *F. kerguelensis* decreased dramatically throughout the cruise. By P3C, abundance and size of *F. kerguelensis* were similar to those at P2,

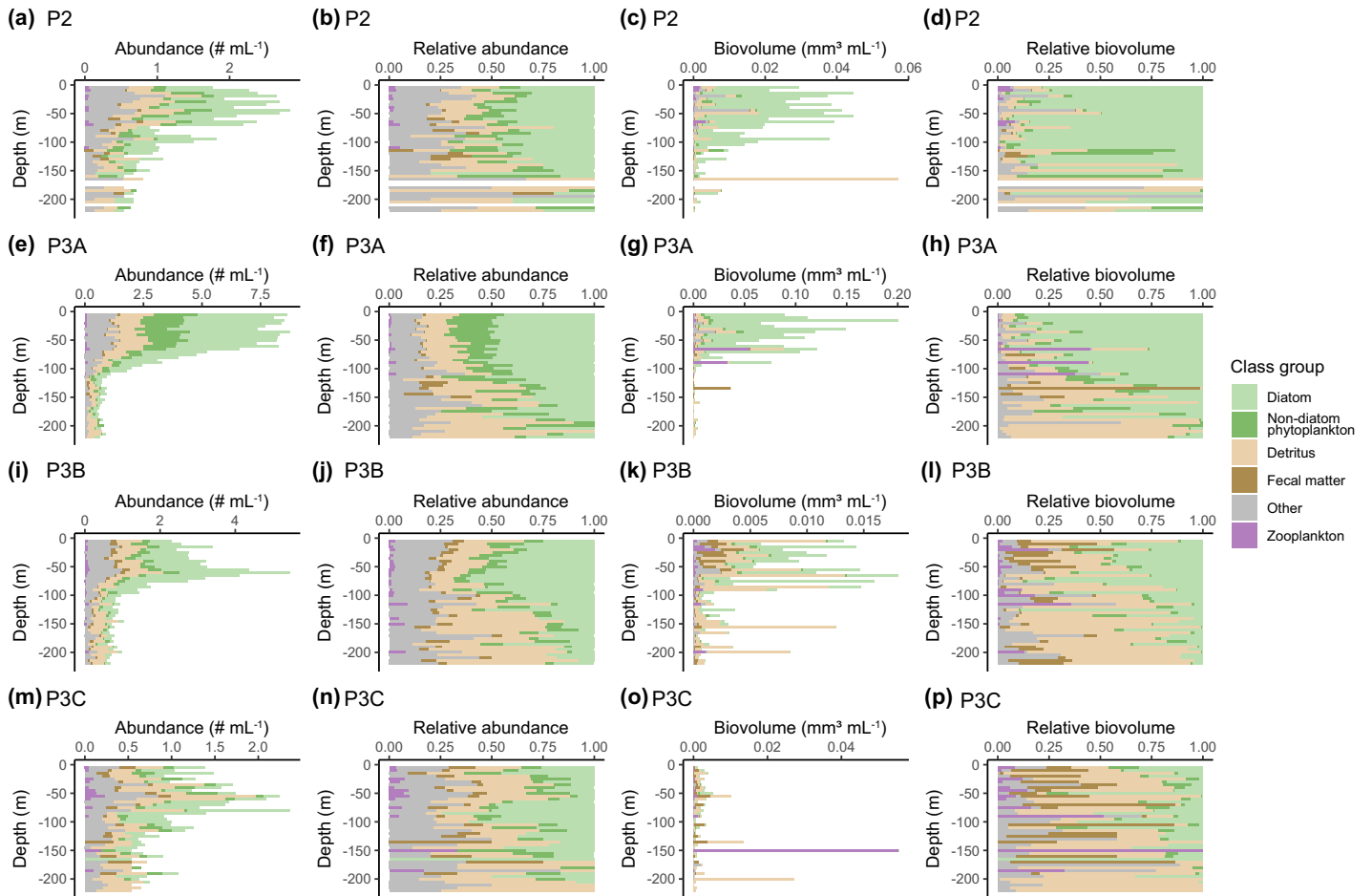


Fig. 3. Vertical profiles of particle abundance and volume during the study period. Abundance (first column), relative abundance (second column), biovolume (third column), and relative biovolume (fourth column) of particles at P2 (a–d) and during P3A (e–h), P3B (i–l), and P3C (m–p). Colors show class groups as indicated in the legend. Note the different x-axes scales.

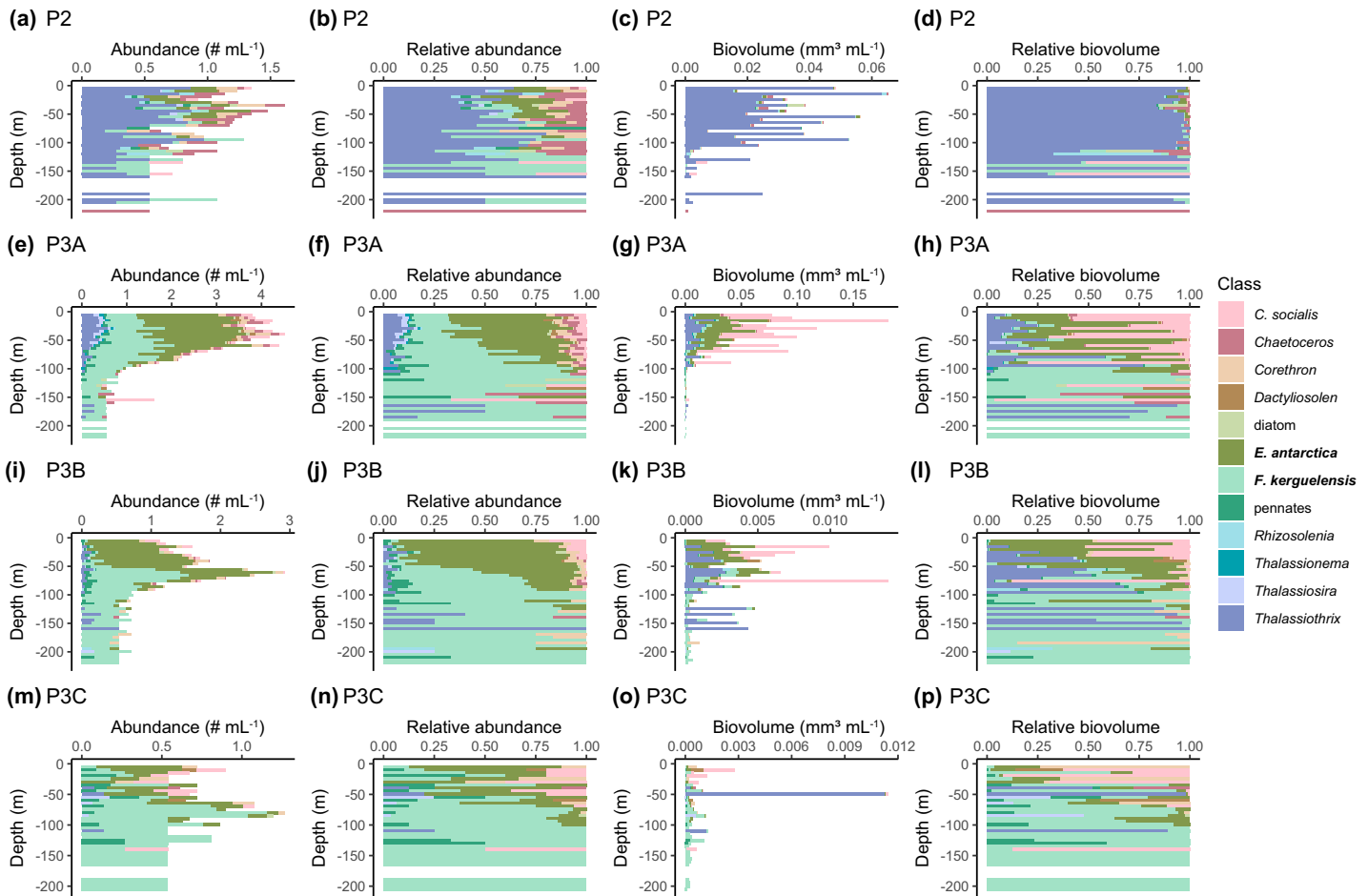


Fig. 4. Vertical profiles of diatom abundance and volume during the study period. Abundance (first column), relative abundance (second column), biovolume (third column), and relative biovolume (fourth column) of diatoms at P2 (a–d) and during P3A (e–h), P3B (i–l), and P3C (m–p). Colors show diatom types as indicated in the legend.

except for a small elevation in the abundance peaking at 75–85 m depth. Similarly, we initially observed large *E. antarctica* throughout the top 50 m (2.0 ± 0.2 chains mL^{-1} with a mean length of 0.31 ± 0.04 mm per chain; Fig. 5e). By the time of P3B, the abundance of *E. antarctica* was still higher than at the non-bloom P2 site (0.8 ± 0.3 vs. 0.2 ± 0.1 chains mL^{-1} , respectively) but their mean length had decreased considerably to 0.10 ± 0.01 mm. By P3C, *E. antarctica* mean length had decreased to 0.06 ± 0.01 mm and abundance was similar to that at P2. While *F. kerguelensis* appeared at depths > 100 m at all stations, *E. antarctica* was only found consistently in the top 100 m at all stations. Overall, at P3, the relative abundances of *F. kerguelensis* increased substantially with depth compared to *E. antarctica*, due to the rapid decrease in abundance of the latter below the mixed layer.

Profiles of detritus showed similar trends in abundance to those of the diatoms (Fig. 5). Abundances were relatively high during P3A in both the top 50 m and below (mean of $1.2 \# \text{L}^{-1}$ and $0.4 \# \text{L}^{-1}$). In contrast, during P3B, P3C and P2, abundances were lower, with mean values of $0.5 \# \text{L}^{-1}$ above 50 m

depth and $0.3 \# \text{L}^{-1}$ below. Unlike the diatoms, detritus size was the same across all profiles and depths, with a mean length of 0.12 ± 0.05 mm (Fig. 5).

Number fluxes, measured by the MSCs, were high for *F. kerguelensis*, with up to 553 chains $\text{cm}^{-2} \text{d}^{-1}$ at 70 m during P3B and an average of 149 ± 156 chains $\text{cm}^{-2} \text{d}^{-1}$ in the top 120 m (Fig. 5). The percentage of sinking chains relative to total abundance was $25\% \pm 37\%$ (Fig. 5i). For *E. antarctica*, the number fluxes were relatively low, with three exceptions, when fluxes were 129 – 389 chains $\text{cm}^{-2} \text{d}^{-1}$ (50–70 m depths; Fig. 5). The percentage of sinking chains relative to total abundance was $3\% \pm 4\%$ (Fig. 5i). Number fluxes are in the range previously observed in the Southern Ocean (Rembauville et al. 2015).

Sinking *F. kerguelensis* chains sampled near the surface (<100 m depth) and upper mesopelagic (100–250 m depth) decreased significantly in size from P3A to P3B (respectively, a change in mean major axis length by 34% from 240 ± 119 to $158 \pm 90 \mu\text{m}$ [$p < 0.001$, $n = 475$] and by 20% from 204 ± 116 to $163 \pm 74 \mu\text{m}$ [$p = 0.015$, $n = 198$]).

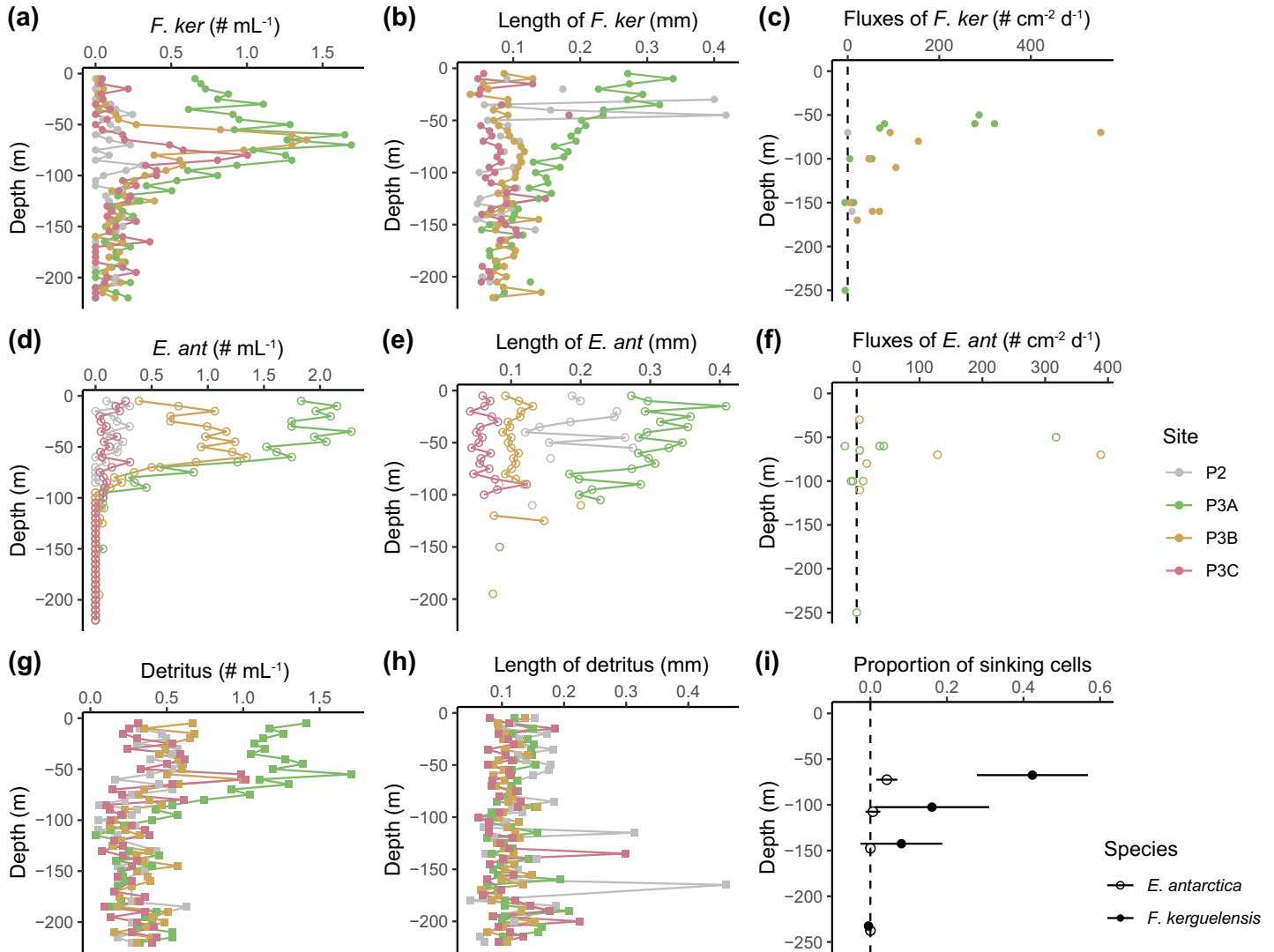


Fig. 5. Vertical profiles of concentration, average length and estimated vertical fluxes of *F. kerguelensis*, *E. antarctica* and detritus during the study period. (a, b, d, e, g, h) Concentration and mean major axis length are based on LISST-Holo images. (c, f) Fluxes are based on MSC measurements. (i) Proportion of sinking cells over total cells (T_0) for *F. kerguelensis* and *E. antarctica* (closed and open circle, respectively). Note change in x-axes. Colors indicate visit: P2 in gray, P3A–P3C in green, orange and red, respectively.

While we found a significant difference in the abundance between the suspended and sinking (T_0 and Tray) fractions for both *F. kerguelensis* and *E. antarctica* (paired t -test; $p < 0.001$ and $p = 0.036$, respectively), there was no statistically significant ($p > 0.16$) difference between the fractions for average length, average volume, and - for *E. antarctica* - in terms of grayscale values. Visual inspection of the images also did not reveal a qualitative difference in the chains. This similarity suggests that, at least for the preserved samples, the sinking and suspended fractions were visually the same.

Gray values of *F. kerguelensis* and *E. antarctica*

The mean grayscale intensities, indicative of full (darker = lower intensity value) and empty (lighter = higher intensity value) frustules, of *F. kerguelensis* were significantly

different (t -test, $p = 0.002$, $n = 769$) for the T_0 and fast-sinking fraction, with a mean of 181 (quartile range: 174–188) and 185 (quartile range: 178–192), respectively (Fig. 6a). Vertical depth profiles of *F. kerguelensis* showed no significant trend with depth for the T_0 fraction (depth range 0–250 m: $p = 0.80$, $R^2 = 0.01$, $n = 65$), whereas the *F. kerguelensis* chains in the fast-sinking fraction became significantly lighter-colored with depth (depth range 0–250 m: $p < 0.01$, $R^2 = 0.02$, $n = 687$) albeit with a high degree of scatter (Fig. 6b,c). There was no significant difference (t -test) in gray intensities over time (i.e., from P3A to P3B) for either the surface (< 100 m depth) or the upper mesopelagic (100–250 m depth).

For *E. antarctica*, mean gray intensities were not significantly different for the T_0 and fast-sinking fractions (t -test, $p = 0.16$, $n = 592$) with an overall mean of 225 (quartile

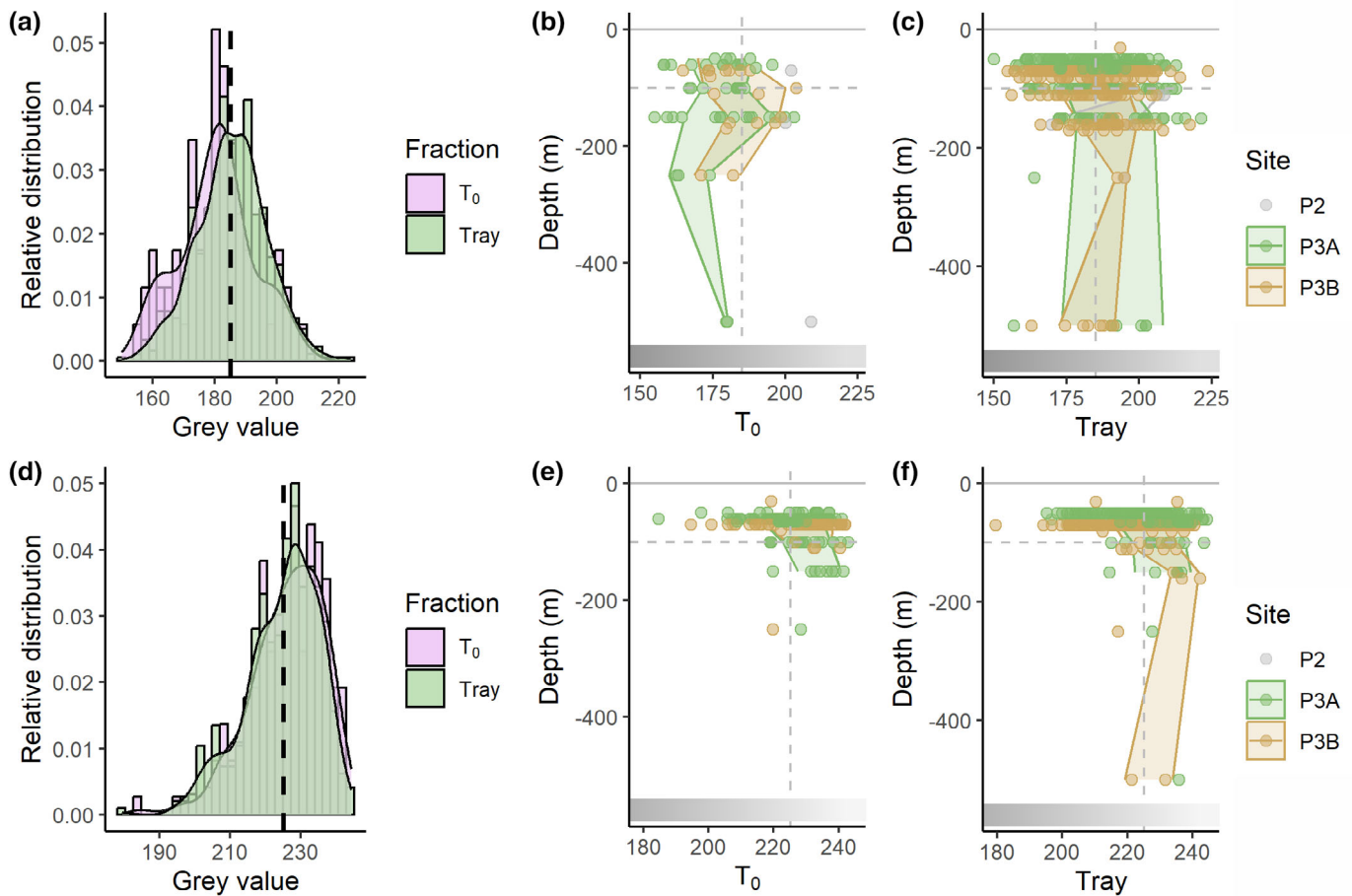


Fig. 6. Gray value of *F. kerguelensis* (a–c) and *E. antarctica* (d–f) chains indicative of full (darker = lower intensity value) and empty (lighter = higher intensity value) frustules. (a, d) Histogram of gray values for each fraction showing the relative frequency distributions for the suspended (T_0 ; purple) and fast-sinking fraction (Tray; green). (b, c, e, f) Vertical depth profiles for the suspended (b: T_0) and fast-sinking fractions (c: Tray). Colors indicate visits (gray = P2, green = P3A, yellow = P3B). Vertical dashed lines indicate median gray value. Color ribbons represent the mean gray value \pm standard deviation for 50-m depth bins (e.g., 25–75 m depth). Means were calculated only for depth bins with at least two particles. Color bars at the bottom show the associated gray shade for each intensity value.

range: 219–233; Fig. 6d). However, vertical profiles showed significantly lighter-colored chains in the T_0 fraction at depths between 100 and 250 m (median value: 232) than near the surface (< 100 m; median value: 226; Wilcoxon test: $p = 0.003$; Fig. 6e). This trend was also significant for the fast-sinking fraction (median values of 231 vs. 227 for deeper and shallow chains, respectively; Wilcoxon test: $p = 0.01$; Fig. 6f).

Photosynthetic efficiency

Across all MSC deployments, Fv/Fm was significantly higher in the suspended fraction after 2 h settling (Top) compared to the fast-sinking fraction (Tray; ANOVA, $p < 0.01$) with means of 0.34 ± 0.05 ($n = 34$) and 0.30 ± 0.05 ($n = 32$), respectively. Values for the T_0 (0.32 ± 0.07 , $n = 33$) and bottom (0.32 ± 0.06 , $n = 34$) fractions were intermediate and statistically indistinguishable from the other fractions. Physiological data across all the measured MSC deployments

were thus consistent with the fastest sinking fraction having a lower Fv/Fm than the suspended fraction.

For the suspended fraction (Top) at P2, Fv/Fm was 0.25 in the upper 100 m and 0.27 ± 0.03 below 100 m depth (Supporting Information Fig. S4). At P3, Fv/Fm of the suspended fraction (Top) increased from 0.35 ± 0.02 (P3B) to 0.41 ± 0.03 (P3C) in the upper 100 m depth. Vertically, the values were similar above and below 100 m depth (0.33 ± 0.04) during P3B. During P3C, Fv/Fm below 100 m depth was notably lower than surface values (0.35 ± 0.06 ; Supporting Information Fig. S4), though this difference likely reflected the increase in Fv/Fm in the surface rather than a decline in the upper mesopelagic.

Phytoplankton communities appeared to be able to maintain photosynthetic efficiency even in prolonged darkness (Supporting Information Fig. S4i). While Fv/Fm appeared to decrease slightly in all incubations over the first 4–6 d, this

trend was only significant for the community sampled during P3B and incubated over 16 d ($p = 0.002$, $R^2 = 0.47$, $n = 17$). Across all incubations, the average daily decrease in Fv/Fm was 0.004 ± 0.001 ($p < 0.001$, $R^2 = 0.37$, $n = 34$). As a result, even after 16 d in darkness, Fv/Fm was still relatively high at ~ 0.31 , down from an initial value of 0.35 ± 0.03 .

Discussion

Our data show a clear change in the vertical composition and abundance of particles throughout the decline of a diatom spring bloom downstream of South Georgia, which was primarily driven by a loss and vertical restructuring of the diatoms *F. kerguelensis* and *E. antarctica*. Both diatom species have been identified as important players in the Southern Ocean

ecosystem, and the following discussion will focus on their differing bloom progression and export dynamics.

Dynamics of *Fragilariopsis kerguelensis*

The depth profiles of *F. kerguelensis* showed peaks in abundance between 50 and 100 m, which moved deeper throughout the cruise (Fig. 7). These deep abundance peaks did not reflect the chlorophyll fluorescence profiles, which showed the typical elevated concentrations throughout the mixed layer, indicating that the distribution of *F. kerguelensis* was driven by different mechanisms to the bulk of the photosynthetically active plankton. The deepening of the abundance peaks also contrasted the slight shallowing of the euphotic zone depth (from 20 ± 4 m during the first visit to 16 ± 2 m

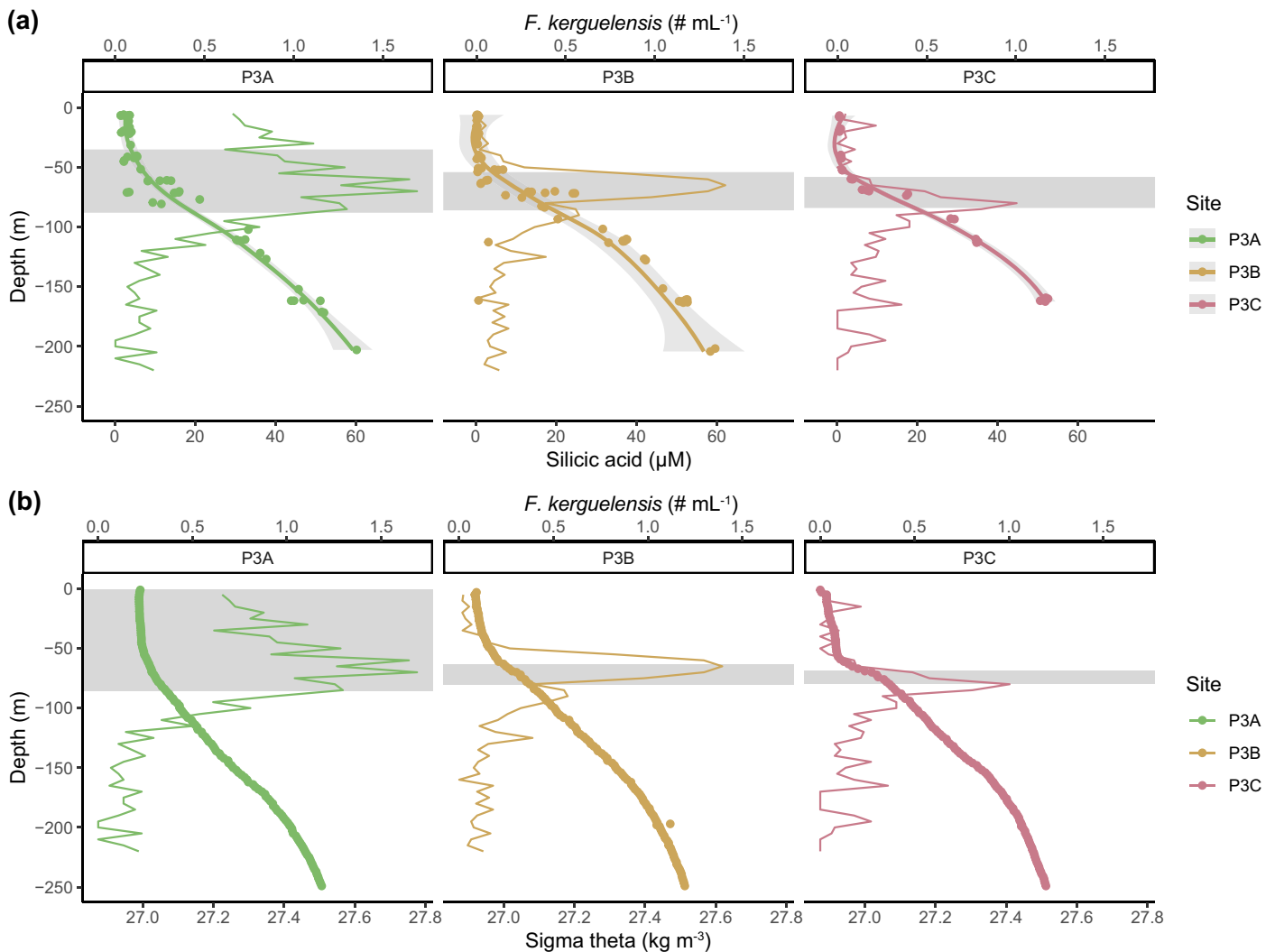


Fig. 7. Vertical profiles of *Fragilariopsis kerguelensis* abundance overlaid on (a) silicic acid profiles and (b) potential density profiles for the three occupations of site P3 (green: P3A, yellow: P3B, red: P3C). In all plots, the thin line shows the depth distribution of *F. kerguelensis* based on LISST-Holo images. (a) Silicic acid was measured from bottle samples (points) and smoothed using the Local Polynomial Regression Fitting. Gray envelope around the line shows the confidence interval of the smoothing function. The gray shaded areas show the depth ranges in which silicic acid concentrations were between 4 and 20 μM . (b) Potential water density anomaly (Sigma theta) profiles based on CTD rosette data. The gray shaded areas show the depth range in which the density anomaly was equivalent to those experienced in the upper 90 m during P3A (i.e., 26.99–27.07 kg m^{-3}).

during the last visit based on 1% PAR relative to 1 m depth), suggesting that light limitation was not a driver of the diatom stratification. Rather, the shift in deep abundance peaks followed the trend in the profiles of nutrients (silicic acid, nitrate and phosphate), suggesting that species stratification could have been driven by nutrient availability. Vertical profiles of dissolved iron showed that surface concentrations were also low (0.03–0.17 nM) and likely of low bioavailability (Ainsworth et al. 2023). However, although there was clear evidence of in situ iron stress throughout the sampled period (Ainsworth et al. 2023), dissolved iron concentrations actually increased slightly as the bloom declined, likely indicative of remineralization (Ainsworth et al. 2023). Moreover, the ferrocline appeared to move shallower (Ainsworth et al. 2023), rather than deeper like the nutricline (compare Fig. 2f,g) and the abundance peak of *F. kerguelensis*. Nitrate and phosphate concentrations remained elevated throughout the study period, suggesting that declining silicic acid, whose concentrations in the mixed layer were higher during P3A and decreased to near-zero by P3B, could have caused *F. kerguelensis* to shift its distribution deeper to where silicic acid concentrations were higher. Visual inspections of the profiles suggest that the abundance peaks corresponded to silicic acid concentrations of 4–20 μM (Fig. 7).

Lafond et al. (2020) proposed an alternative mechanism, suggesting that the vertical abundance profiles of heavier diatoms like *F. kerguelensis* (and *E. antarctica*) can be caused by sinking and accumulation in the pycnocline. During our study, the change of the near-surface water density profiles could indeed also explain the observed abundance stratification of *F. kerguelensis*. The warming of the near-surface ocean during our cruise caused a decrease in the water density. It is hence reasonable that *F. kerguelensis* was conditioned to achieve neutral cell density in the mixed layer during P3A and, when the water density of this near-surface zone decreased, the diatom chains had excess density that caused them to sink until they reached the depth of the higher water density (Fig. 7). Such a mechanism would imply that *F. kerguelensis* has a limited ability to quickly increase buoyancy, unlike shown for other diatom species (e.g., *Rhizosolenia*; Villareal et al. 2014).

The drastic change in water density profiles, coupled to *F. kerguelensis*' possibly low density plasticity, could further explain the high fluxes of *F. kerguelensis* chains we observed in the near-surface ocean: These fluxes may capture the restructuring of the water column following the warming of the surface temperature (hence decrease in water density). Moreover, the tight coupling of a chain's density to relatively narrow water density bands can explain the rapid flux attenuation as the water density gradient at P3 was steep and would have acted as a strong physical barrier.

While our data are inconclusive on whether the primary driver for the vertical structure of *F. kerguelensis* was silicic acid availability and/or water density gradients, *F. kerguelensis* was

likely nutrient (silicon and/or iron) stressed (Ainsworth et al. 2023). In addition to the overall community responses following iron resupply (Ainsworth et al. 2023), nutrient stress can also influence chain length. During the Southern Ocean Iron Release Experiment (SOIREE), chain length of *F. kerguelensis* doubled as a response to iron enrichment (Gall et al. 2001). Similarly, *Fragilariopsis* sp. along the Indian coast has also been observed to increase its chain length dramatically under favorable growth conditions (in this case high nitrate concentrations; Jyothibabu et al. 2018). Here, we observed a significant shortening of the chains in the surface (< 100 m depth; in both the T_0 and fast-sinking factions) as the bloom declined, which could indicate nutrient stress or—at least—unfavorable growth conditions due to poor availability of iron, silicic acid, or both.

While the above studies propose a lengthening in chains, which can be achieved by growth, our results showed an apparent shortening, which points toward either the breaking up of chains or the production of new, shorter chains. In the near-surface ocean, we predominantly “lost” chains of a length 200–600 μm and instead recorded a peak in chains between 70 and 130 μm (corresponding to approximately 11–17 frustules). As there was no associated export flux of longer chains (albeit, this result is based on MSC samples, whose handling during storage and analysis may have caused fragmentation), and the overall abundance of *F. kerguelensis* chains decreased, it seems unlikely that the change in chain length distribution was driven by either the sinking of long chains or the new production of short chains (i.e., new growth). Rather, we propose that long chains either actively or passively broke into smaller fragments.

Diatom chain length has been shown to decrease in the presence of copepod grazers (O'Connors, Small, and Donaghay 1976; Deason 1980; Bergkvist et al. 2012). While the reduction in chain length was originally thought to be a result of physical fragmentation by copepods (Martin 1970; O'Connors, Small, and Donaghay 1976; Deason 1980), later studies revealed that diatoms (in this case *Skeletonema*) actively reduce chain length in response to chemical cues released when copepods feed (Bjærke et al. 2015), both on other diatoms or other phytoplankton (Bergkvist et al. 2012). This response is likely an adaptation to avoid predation by mesozooplankton grazers as many copepods exhibit size-dependent prey selection with some species preferring longer diatom chains to shorter chains or single cells (Richman and Rogers 1969; Meyer et al. 2002). Subsequent models supported the notion that chain length can be actively controlled by diatoms (here *Chaetoceros* and *Phaeodactylum*) in response to environmental conditions (Gherardi et al. 2016). During our study, mesozooplankton biomass was highest during P3A and decreased thereafter (Cook et al. 2023). While there could be a time lag between grazer activity and an active diatom-induced reduction in chain length, both Bergkvist et al. (2012) and Bjærke et al. (2015) observed a response in diatom chain length to the presence of predators within 48 h. Our visits

to P3 were each ~ 7 d long, so we would expect to capture any prey–predator response chain length already during each of our visits. Hence, the lack of correlation between copepod abundance and chain length suggests that chain shortening was not primarily driven as a response to grazing.

Another explanation is physical disturbance. In *F. kerguelensis* cultures, chain length can vary considerably depending on the care of handling (Hassler and Schoemann 2009). Similar physical disturbance could occur in the ocean during storms. During our cruise, a strong storm hit the study site (P3) between the visits P3A and P3B with strong winds that prohibited any research work overboard. Possibly, storm-induced turbulent kinetic energy may have reached levels that lead to small-scale eddies as small as $100\ \mu\text{m}$ (aka a Kolmogorov length scale of $100\ \mu\text{m}$). Objects larger than $100\ \mu\text{m}$ could hence experience high shear stress and may break into pieces smaller than this length scale. The turbulent kinetic energy associated with a Kolmogorov length scale of $100\ \mu\text{m}$ is $10^{-2}\ \text{W kg}^{-1}$. Such high levels of turbulent kinetic energy are common in very energetic areas such as tidal channels, bottom boundary layers (Smyth and Moum 2019) and coastal regions during strong storms (Ma et al. 2020), and they have also recently been observed in the Southern Ocean (Ferris et al. 2022). A prerequisite for turbulent-flow-induced breakage is that diatom chains are relatively rigid and susceptible to breakage. Some species, such as *Thalassiosira* are very flexible and can resist breakage under high shear stress (Nguyen and Fauci 2014), others (e.g., *Lithodesmium undulatum* and *Stephanopyxis turris*) are susceptible to breaking at relatively low flow speeds ($<0.01\ \text{m s}^{-1}$) when nutrient limited (Young et al. 2012). Unfortunately, we could not find any information on the rigidity of *F. kerguelensis*; they were, however, likely nutrient stressed and hence more prone to breaking. Overall, we suggest that the size distribution of *F. kerguelensis* toward the end of our study period was likely driven primarily by a combination of diminishing chain growth owing to nutrient limitation, and increased chain breakage owing to storm-induced turbulence in the upper ocean.

The high flux of *F. kerguelensis* (on average 25% of the standing stock was found to be sinking) suggests that the main loss process was sinking of chains from the upper ocean. This suggestion is further supported by the relatively high numbers of *F. kerguelensis* captured throughout the upper mesopelagic, where they were observed in almost all depth bins (Fig. 4). Sediment trap samples from 2000 m depth also reported that up to 60% of the diatoms found in the traps were *F. kerguelensis* (Manno et al. 2022). A similar observation was made during the European Iron Fertilization Experiment (EIFEX), where a steady flux of *F. kerguelensis* below 100 m depth was implied from abundance profiles (Assmy et al. 2013). The thick, silicified frustules resistant to mechanical deformation and breakage (Hamm et al. 2003; Hoffmann, Peeken, and Lochte 2007) may protect from copepod grazing (Smetacek, Assmy, and Henjes 2004; Assmy et al. 2013) and could lead to a low-level, constant mortality rate and subsequent flux (Assmy et al. 2013).

In our study, while total POC flux decreased from the first to the second visit at P3 (i.e., from P3A to P3B; Giering et al. 2023), the flux of *F. kerguelensis* increased slightly, potentially reflecting the loss of *F. kerguelensis* from the upper ocean to depth via sinking when considering a time lag (Giering et al. 2017). The opposing trends of POC fluxes and *F. kerguelensis* fluxes suggests that either *F. kerguelensis* frustules carried less carbon during P3B (e.g., because of being empty or smaller) and/or that the POC flux was dominated by other particles. Though we did not measure cell carbon content, *F. kerguelensis* chains indeed became smaller and lighter in color—indicative of more empty frustules, that is, less carbon content—from P3A to P3B to P3C (for the latter transition only size information is available). A decrease in chain size could further result in a reduction in sinking velocity hence flux, though this effect may be partly offset by an increase in cell density (i.e., loss of buoyancy) due to a larger proportion of empty frustules. At the same time, the contribution of detritus to the total particle population at depth increased. Overall, the *F. kerguelensis* appeared to become less important for carbon transport from the near-surface to the upper mesopelagic as the bloom decline progressed. This interpretation is supported by direct flux measurements of POC and biogenic silica during our study, which suggest that these two components are decoupled (Williams et al. 2024) with POC-rich particles—specifically fecal pellets—dominating deep fluxes (2000 m depth; Manno et al. 2022).

Dynamics of *E. antarctica*

While we were able to get a comprehensive insight into the dynamics of *F. kerguelensis*, interpretation is more difficult for *E. antarctica* as they seemed to have simply disappeared without an indication of vertical redistribution. As for *F. kerguelensis*, the rapid decrease in abundance appeared to be linked to the decrease in silicic acid concentrations and water density changes after P3A. Similarly, we observed a decrease in the size of *E. antarctica*, potentially also a response to the changing environmental conditions. However, we did not observe noticeable vertical fluxes of *E. antarctica* (on average only 3% of the standing stock was found to be within the fastest sinking fractions), and we only rarely captured any *E. antarctica* chains or cells below 100 m depth, suggesting that *E. antarctica* were either efficiently grazed and hence recycled in the surface ocean, changed appearance so that we were unable to recognize them, or were exported and transferred so rapidly that we were unable to detect changes in vertical structure. The latter process appears unlikely as the deep sediment trap samples at ~ 2000 m depth collected only small numbers of *E. antarctica* (Manno et al. 2022). A more likely explanation for the decrease in abundance is hence a combination of grazing and moderate levels of export that followed a different progression to those of *F. kerguelensis*. Different flux behaviors for these two diatoms have also been observed, based on deep sediment traps, around the Crozet Island (Salter et al. 2012). There, deep fluxes of *E. antarctica* were almost

entirely composed of resting spores of this species (Salter et al. 2012). Resting spore formation of several diatom species has been suggested to be triggered by nutrient stress (Kuwata, Hama, and Takahashi 1993; Peters and Thomas 1996), and spores may hence have been formed during our cruise when silicate concentrations became limiting. As resting spores, which are typically single cells (Fryxell, Villareal, and Doucette 1981), of *E. antarctica* are small ($< 100 \mu\text{m}$), we may have been unable to positively identify these by our methods.

The significantly lighter-colored chains at depth indicate that empty cells were preferentially exported. This observation is in line with previous studies over the Kerguelen Plateau that observed an increasing percentage of empty frustules with depth (e.g., Lasbleiz et al. 2016) and their presence in sediment traps (Rembauville et al. 2015). Though, the latter study reported that fluxes of *E. antarctica* were always dominated by full cells, unlike those of other diatom species such as *F. kerguelensis*, *Fragilariopsis separanda*, *Pseudo-nitzschia* spp, *Thalassionema nitzschioides* and small centrics. We also observed that the suspended and sinking fractions were visually the same. Overall, *E. antarctica* was concluded to not be a major driver of carbon fluxes over the Kerguelen Plateau (Rembauville et al. 2015), consistent with our findings near South Georgia and those based on deep sediment traps at our site (Manno et al. 2022).

Live diatoms in the upper mesopelagic zone

Measured levels of the apparent photosynthetic efficiency (Fv/Fm) were relatively high throughout the upper mesopelagic (Supporting Information Fig. S4), being comparable to those in the surface ocean, suggesting that phytoplankton transported to these depths have either arrived here fairly recently or can maintain photosynthetic efficiency for a while. Based on our image data and size-fractionated chlorophyll data (Ainsworth et al. 2023), the near-surface phytoplankton community remained dominated by cells $> 10 \mu\text{m}$ throughout our sampling at P3, most likely diatoms due to consistently high cell counts (Ainsworth et al. 2023). Diatoms are known to be capable of surviving for extended periods in the dark. Based on bottle incubations, Peters and Thomas (1996) showed that viability of diatoms remained high even after > 100 d in the darkness, returning to maximal growth values within a few days of being returned to the light. This resilience to extended darkness likely explains why viable photosynthetic cells, predominantly diatoms, have been observed between 2000 and 4000 m depth throughout the global ocean (Agusti et al. 2015). Our experimental data support these observations, showing that surface phytoplankton communities during our study, which were dominated by diatoms, remained photosynthetically viable for over 2 weeks when incubated in the dark (Supporting Information Fig. 4i).

Nonetheless, the most rapidly sinking particulate fractions collected within the MSC displayed significantly lower photosynthetic efficiency compared to the suspended phytoplankton. Considering the notable role of *F. kerguelensis* for sinking

fluxes (Rigual-Hernández et al. 2015; Manno et al. 2022), one may expect these results to imply that fluxes were driven by nutrient stressed *F. kerguelensis*. However, while *F. kerguelensis* dominated the fast-sinking fraction in the upper 150 m, their contribution to the sinking fractions below 200 m was smaller, indicating that the lower Fv/Fm values at these depths do not simply reflect the photosynthetic efficiency of *F. kerguelensis*. Rather, both *F. kerguelensis* abundance and Fv/Fm were elevated in the suspended fractions relative to the fast-sinking fraction (Supporting Information Fig. S4 and S5), which could imply that *F. kerguelensis* at these depths were viable.

The systematically lower Fv/Fm values combined with highly variable phytoplankton community composition in the tray fractions indicate that sinking particles comprised an assemblage of relatively more senescent or stressed phytoplankton. Further supporting this notion is that much of the marine snow we observed in the sinking fraction appeared to be detritus (particularly relatively dense aggregates containing phytoplankton cells) and loosely aggregated phytoplankton cells that appeared to be connected by transparent matter (e.g., transparent exopolymer particles).

Overall, we conclude that live diatoms were a significant contributor to export and particulate biomass in the upper mesopelagic zone. This observation begs the question whether live diatoms need explicit consideration in understanding and modeling the Southern Ocean biological pump. For example, the silica frustule of live cells will presumably be relatively resistant to degradation due to an intact organic coating, which would influence the silica cycle. In addition, live diatoms would be expected to continue respiring but will not be “remineralized” in the normally used sense (i.e., no cellular breakup, limited release of nitrogen, silica, iron, etc. will occur). Finally, for mesopelagic carbon budgets (e.g., Giering et al. 2014, 2023), deep diatom respiration by suspended cells would not be associated with a direct loss in fluxes, leading to an apparent imbalance of carbon supply and respiration.

Conclusion

We here describe three consecutive snapshots of plankton processes during the declining phase of a diatom spring bloom in an iron-fertilized region of the Southern Ocean. We reveal a clear decoupling between the surface population and the exported material, with the surface community persistently containing a taxonomically distinct assemblage relative to the upper mesopelagic zone. As the bloom declined, the surface community, which was initially dominated by diatoms, transitioned to being dominated by detrital material. In the upper mesopelagic, only one of the diatom species observed in the surface community (*F. kerguelensis*) was abundant. The reasons underpinning this vertical decoupling are not clear; however, these observations underline the need to understand the species-specific controls of phytoplankton populations to understand the carbon export processes.

Author Contributions

SLCG: Conceptualization, methodology, investigation, formal analysis, validation, visualization, writing, funding acquisition, project administration, resources, supervision. **FC:** Investigation, writing. **MHI:** Investigation. **ZL:** Data curation, formal analysis, methodology, software. **OM:** Investigation. **CMM:** Investigation, validation, supervision, writing, funding acquisition. **MO:** Methodology. **UP:** Resources. **AJP:** Investigation, validation, writing, funding acquisition. **ER:** Methodology. **TT:** Resources. **RS:** Funding acquisition.

Acknowledgments

We thank Richard Lampitt and Kevin Saw for the deployment of the Red Camera Frame, and Mark Stinchcombe for the nutrient analysis during DY086. We thank the captain and crew of the RSS Discovery during DY086 as well as the South Atlantic Environmental Research Institute (SAERI) for their help during mobilization. We thank all scientists within the COMICS program for comments and discussion. Finally, we thank the editors and reviewers for their constructive feedback. This work was funded by the Natural Environment Research Council through the COMICS project (Controls over Ocean Mesopelagic Interior Carbon Storage; NE/M020835/1 and NE/M02072X/1). SLCG and ZL were supported through the ANTICS project, receiving funding from the European Research Council (ERC) under the European Union's Horizon 2020 research and innovation program (Grant Agreement 950212). ER was supported by the University of California, Santa Barbara, Earth Research Institute (150RE1). Sample analysis and collaboration between SLCP and UP was partly supported by the Ocean Frontier Institute, through an award from the Canada First Research Excellence Fund, and through the Canada Chair Program to UP.

Conflicts of Interest

None declared.

References

- Agusti, S., J. I. González-Gordillo, D. Vaqué, et al. 2015. "Ubiquitous Healthy Diatoms in the Deep Sea Confirm Deep Carbon Injection by the Biological Pump." *Nature Communications* 6: 7608. <https://doi.org/10.1038/ncomms8608>.
- Ainsworth, J., A. J. Poulton, M. C. Lohan, M. C. Stinchcombe, A. J. M. Lough, and C. M. Moore. 2023. "Iron Cycling during the Decline of a South Georgia Diatom Bloom." *Deep Sea Research Part II: Topical Studies in Oceanography* 208: 105269. <https://doi.org/10.1016/j.dsr2.2023.105269>.
- Allredge, A. L., and M. W. Silver. 1988. "Characteristics, Dynamics and Significance of Marine Snow." *Progress in Oceanography* 20: 41–82. [https://doi.org/10.1016/0079-6611\(88\)90053-5](https://doi.org/10.1016/0079-6611(88)90053-5).
- Allen, C. S. 2014. "Proxy Development: A New Facet of Morphological Diversity in the Marine Diatom *Eucampia Antarctica* (Castracane) Mangin." *Journal of Micropalaeontology* 33: 131–142. <https://doi.org/10.1144/jmpaleo2013-025>.
- Armand, L. K., V. Cornet-Barthaux, J. Mosseri, and B. Quéguiner. 2008. "Late Summer Diatom Biomass and Community Structure on and Around the Naturally Iron-Fertilised Kerguelen Plateau in the Southern Ocean." *Deep Sea Research Part II: Topical Studies in Oceanography* 55: 653–676. <https://doi.org/10.1016/j.dsr2.2007.12.031>.
- Assmy, P., V. Smetacek, M. Montresor, et al. 2013. "Thick-Shelled, Grazer-Protected Diatoms Decouple Ocean Carbon and Silicon Cycles in the Iron-Limited Antarctic Circumpolar Current." *Proceedings of the National Academy of Sciences* 110: 20633–20638. <https://doi.org/10.1073/pnas.1309345110>.
- Bergkvist, J., P. Thor, H. H. Jakobsen, S.-Å. Wängberg, and E. Selander. 2012. "Grazer-Induced Chain Length Plasticity Reduces Grazing Risk in a Marine Diatom." *Limnology and Oceanography* 57: 318–324. <https://doi.org/10.4319/lo.2012.57.1.0318>.
- Bjærke, O., P. R. Jonsson, A. Alam, and E. Selander. 2015. "Is Chain Length in Phytoplankton Regulated to Evade Predation?" *Journal of Plankton Research* 37: 1110–1119. <https://doi.org/10.1093/plankt/fbv076>.
- Blain, S., B. Quéguiner, L. Armand, et al. 2007. "Effect of Natural Iron Fertilization on Carbon Sequestration in the Southern Ocean." *Nature* 446: 1070–1074. <https://doi.org/10.1038/nature05700>.
- Borrione, I., and R. Schlitzer. 2013. "Distribution and Recurrence of Phytoplankton Blooms Around South Georgia, Southern Ocean." *Biogeosciences* 10: 217–231. <https://doi.org/10.5194/bg-10-217-2013>.
- Boyd, P. W., A. J. Watson, C. S. Law, et al. 2000. "A Mesoscale Phytoplankton Bloom in the Polar Southern Ocean Stimulated by Iron Fertilization." *Nature* 407: 695–702. <https://doi.org/10.1038/35037500>.
- Buesseler, K. O. 1998. "The Decoupling of Production and Particulate Export in the Surface Ocean." *Global Biogeochemical Cycles* 12: 297–310. <https://doi.org/10.1029/97GB03366>.
- Burd, A. B., and G. A. Jackson. 2009. "Particle Aggregation." *Annual Review of Marine Science* 1: 65–90. <https://doi.org/10.1146/annurev.marine.010908.163904>.
- Cook, K. B., A. Belcher, D. R. Bondyale-Juez, et al. 2023. "Carbon Budgets of Scotia Sea Mesopelagic Zooplankton and Micronekton Communities during Austral Spring." *Deep Sea Research Part II: Topical Studies in Oceanography* 210: 105296. <https://doi.org/10.1016/j.dsr2.2023.105296>.
- Cullen, J. J., and R. F. Davis. 2003. "The Blank Can Make a Big Difference in Oceanographic Measurements." *Limnology and Oceanography Bulletin* 12: 29–35. <https://doi.org/10.1002/lob.200312229>.
- de Baar, H. J. W. 2005. "Synthesis of Iron Fertilization Experiments: From the Iron Age in the Age of Enlightenment."

- Journal of Geophysical Research* 110: C09S16. <https://doi.org/10.1029/2004JC002601>.
- Deason, E. E. 1980. "Grazing of *Acartia Hudsonica* (*A. clausi*) on *Skeletonema Costatum* in Narragansett Bay (USA): Influence of Food Concentration and Temperature." *Marine Biology* 60: 101–113. <https://doi.org/10.1007/BF00389153>.
- Ferris, L., D. Gong, C. A. Clayson, et al. 2022. "Shear Turbulence in the High-Wind Southern Ocean Using Direct Measurements." *Journal of Physical Oceanography* 52: 2325–2341. <https://doi.org/10.1175/JPO-D-21-0015.1>.
- Froneman, P. W., E. A. Pakhomov, and R. K. Laubscher. 1997. "Microphytoplankton Assemblages in the Waters Surrounding South Georgia, Antarctica during Austral Summer 1994." *Polar Biology* 17: 515–522. <https://doi.org/10.1007/s003000050150>.
- Fryxell, G. A. 1991. "Comparison of Winter and Summer Growth Stages of the Diatom *Eucampia antarctica* from the Kerguelen Plateau and South of the Antarctic Convergence Zone." *Proceeding of the Ocean Drilling Program, Scientific Results* 119: 675–685. <https://doi.org/10.2973/odp.proc.sr.119.139.1991>.
- Fryxell, G. A., T. A. Villareal, and G. Doucette. 1981. "Diatom Resting Spores and Agulhas Collections." *Antarctic Journal of the United States* 16: 128–130.
- Gall, M. P., P. W. Boyd, J. Hall, K. A. Safi, and H. Chang. 2001. "Phytoplankton Processes. Part 1: Community Structure During the Southern Ocean Iron RElease Experiment (SOIREE)." *Deep Sea Research Part II: Topical Studies in Oceanography* 48: 2551–2570. [https://doi.org/10.1016/S0967-0645\(01\)00008-X](https://doi.org/10.1016/S0967-0645(01)00008-X).
- Gherardi, M., A. Amato, J.-P. Bouly, et al. 2016. "Regulation of Chain Length in Two Diatoms as a Growth-Fragmentation Process." *Physical Review E* 94: 022418. <https://doi.org/10.1103/PhysRevE.94.022418>.
- Giering, S. L. C., R. Sanders, A. P. Martin, et al. 2017. "Particle Flux in the Oceans: Challenging the Steady State Assumption." *Global Biogeochemical Cycles* 31: 159–171. <https://doi.org/10.1002/2016GB005424>.
- Giering, S. L. C., R. Sanders, A. P. Martin, et al. 2016. "High export via small particles before the onset of the North Atlantic spring bloom." *Journal of Geophysical Research* 121: 6929–6945. <https://doi.org/10.1002/2016JC012048>.
- Giering, S. L. C., S. Steigenberger, E. P. Achterberg, R. Sanders, and D. J. Mayor. 2012. "Elevated Iron to Nitrogen Recycling by Mesozooplankton in the Northeast Atlantic Ocean." *Geophysical Research Letters* 39:L12608. <https://doi.org/10.1029/2012GL051776>.
- Giering, S. L. C., R. Sanders, R. S. Lampitt, et al. 2014. "Reconciliation of the Carbon Budget in the Ocean's Twilight Zone." *Nature* 507: 480–483. <https://doi.org/10.1038/nature13123>.
- Giering, S. L. C., R. Sanders, S. Blackbird, et al. 2023. "Vertical Imbalance in Organic Carbon Budgets Is Indicative of a Missing Vertical Transfer During a Phytoplankton Bloom Near South Georgia (COMICS)." *Deep Sea Research Part II: Topical Studies in Oceanography* 209: 105277. <https://doi.org/10.1016/j.dsr2.2023.105277>.
- Graham, G. W., and W. A. M. Nimmo Smith. 2010. "The Application of Holography to the Analysis of Size and Settling Velocity of Suspended Cohesive Sediments." *Limnology and Oceanography: Methods* 8: 1–15. <https://doi.org/10.4319/lom.2010.8.1>.
- Gruber, N., P. Landschützer, and N. S. Lovenduski. 2019. "The Variable Southern Ocean Carbon Sink." *Annual Review of Marine Science* 11: 159–186. <https://doi.org/10.1146/annurev-marine-121916-063407>.
- Hamm, C. E., R. Merkel, O. Springer, et al. 2003. "Architecture and Material Properties of Diatom Shells Provide Effective Mechanical Protection." *Nature* 421: 841–843. <https://doi.org/10.1038/nature01416>.
- Hassler, C. S., and V. Schoemann. 2009. "Interactive comment on 'Bioavailability of organically bound Fe to model phytoplankton of the Southern Ocean'." *Biogeosciences Discussions* 6: S1179–S1188. <https://doi.org/10.5194/bg-6-2281-2009>.
- Hoffmann, L. J., I. Peeken, and K. Lochte. 2007. "Effects of Iron on the Elemental Stoichiometry During EIFEX and in the Diatoms *Fragilariopsis kerguelensis* and *Chaetoceros dichaeta*." *Biogeosciences* 4: 569–579. <https://doi.org/10.5194/bg-4-569-2007>.
- Ikeda, T. 1985. "Metabolic Rates of Epipelagic Marine Zooplankton as a Function of Body Mass and Temperature." *Marine Biology* 85: 1–11. <https://doi.org/10.1007/BF00396409>.
- Jyothibabu, R., N. Arunpandi, C. Karnan, et al. 2018. "*Fragilariopsis* Sp. Bloom Causes Yellowish-Brown Waters off Alappuzha, South-Central Kerala Coast, India, during the Mud Bank-Upwelling Phase." *Current Science* 115: 152–159. <https://doi.org/10.18520/cs/v115/i1/152-159>.
- Kagami, M., A. de Bruin, B. W. Ibelings, and E. van Donk. 2007. "Parasitic Chytrids: Their Effects on Phytoplankton Communities and Food-Web Dynamics." *Hydrobiologia* 578: 113–129. <https://doi.org/10.1007/s10750-006-0438-z>.
- Kemp, A. E. S., R. B. Pearce, I. Grigorov, et al. 2006. "Production of Giant Marine Diatoms and their Export at Oceanic Frontal Zones: Implications for Si and C Flux from Stratified Oceans." *Global Biogeochemical Cycles* 20: GB4S04. <https://doi.org/10.1029/2006GB002698>.
- Klawonn, I., S. Van den Wyngaert, M. H. Iversen, et al. 2023. "Fungal Parasitism on Diatoms Alters Formation and Biophysical Properties of Sinking Aggregates." *Communications Biology* 6: 1–14. <https://doi.org/10.1038/s42003-023-04453-6>.
- Korb, R. E., M. J. Whitehouse, A. Atkinson, and S. E. Thorpe. 2008. "Magnitude and Maintenance of the Phytoplankton Bloom at South Georgia: A Naturally Iron-Replete Environment." *Marine Ecology Progress Series* 368: 75–91. <https://doi.org/10.3354/meps07525>.
- Kranzler, C. F., J. W. Krause, M. A. Brzezinski, et al. 2019. "Silicon Limitation Facilitates Virus Infection and Mortality of Marine

- Diatoms." *Nature Microbiology* 4: 1790–1797. <https://doi.org/10.1038/s41564-019-0502-x>.
- Kuwata, A., T. Hama, and M. Takahashi. 1993. "Ecophysiological Characterization of Two Life Forms, Resting Spores and Resting Cells, of a Marine Planktonic Diatom, *Chaetoceros Pseudocurvisetus*, Formed under Nutrient Depletion." *Marine Ecology Progress Series* 102: 245–255. <https://doi.org/10.3354/meps102245>.
- Lafond, A., K. Leblanc, J. Legras, V. Cornet, and B. Quéguiner. 2020. "The Structure of Diatom Communities Constrains Biogeochemical Properties in Surface Waters of the Southern Ocean (Kerguelen Plateau)." *Journal of Marine Systems* 212: 103458. <https://doi.org/10.1016/j.jmarsys.2020.103458>.
- Lasbleiz, M., K. Leblanc, L. K. Armand, et al. 2016. "Composition of Diatom Communities and their Contribution to Plankton Biomass in the Naturally Iron-Fertilized Region of Kerguelen in the Southern Ocean." *FEMS Microbiology Ecology* 92: fiw171. <https://doi.org/10.1093/femsec/fiw171>.
- Liu, Z., S. Giering, T. Thevar, N. Burns, M. Ockwell, and J. Watson. 2023. "Machine-Learning-Based Size Estimation of Marine Particles in Holograms Recorded by a Submersible Digital Holographic Camera." *OCEANS 2023 - Limerick, Limerick, Ireland, 2023*, 1–8. <https://doi.org/10.1109/OCEANSLimerick52467.2023.10244456>.
- Ma, H., D. Dai, J. Guo, and F. Qiao. 2020. "Observational Evidence of Surface Wave-Generated Strong Ocean Turbulence." *Journal of Geophysical Research, Oceans* 125: e2019JC015657. <https://doi.org/10.1029/2019JC015657>.
- Manno, C., G. Stowasser, P. Enderlein, S. Fielding, and G. A. Tarling. 2015. "The Contribution of Zooplankton Faecal Pellets to Deep-Carbon Transport in the Scotia Sea (Southern Ocean)." *Biogeosciences* 12: 1955–1965. <https://doi.org/10.5194/bg-12-1955-2015>.
- Manno, C., G. Stowasser, S. Fielding, B. Apeland, and G. A. Tarling. 2022. "Deep Carbon Export Peaks Are Driven by Different Biological Pathways during the Extended Scotia Sea (Southern Ocean) Bloom." *Deep Sea Research Part II: Topical Studies in Oceanography* 205: 105183. <https://doi.org/10.1016/j.dsr2.2022.105183>.
- Martin, J. H. 1970. "Phytoplankton-Zooplankton Relationships in Narragansett Bay. Iv. The Seasonal Importance of Grazing1." *Limnology and Oceanography* 15: 413–418. <https://doi.org/10.4319/lo.1970.15.3.0413>.
- Meyer, B., X. Irigoien, M. Graeve, R. Head, and R. Harris. 2002. "Feeding Rates and Selectivity Among Nauplii, Copepodites and Adult Females of *Calanus finmarchicus* and *Calanus helgolandicus*." *Helgoland Marine Research* 56: 169–176. <https://doi.org/10.1007/s10152-002-0105-3>.
- Moore, C. M., S. Seeyave, A. E. Hickman, et al. 2007. "Iron-Light Interactions during the CROZet Natural Iron Bloom and EXport Experiment (CROZEX) I: Phytoplankton Growth and Photophysiology." *Deep Sea Research Part II: Topical Studies in Oceanography* 54: 2045–2065. <https://doi.org/10.1016/j.dsr2.2007.06.011>.
- Mosseri, J., B. Quéguiner, L. Armand, and V. Cornet-Barthaux. 2008. "Impact of Iron on Silicon Utilization by Diatoms in the Southern Ocean: A Case Study of Si/N Cycle Decoupling in a Naturally Iron-Enriched Area." *Deep Sea Research Part II: Topical Studies in Oceanography* 55: 801–819. <https://doi.org/10.1016/j.dsr2.2007.12.003>.
- Nguyen, H., and L. Fauci. 2014. "Hydrodynamics of Diatom Chains and Semiflexible Fibres." *Journal of the Royal Society Interface* 11: 20140314. <https://doi.org/10.1098/rsif.2014.0314>.
- Nielsdóttir, M. C., T. S. Bibby, C. M. Moore, et al. 2012. "Seasonal and Spatial Dynamics of Iron Availability in the Scotia Sea." *Marine Chemistry* 130–131: 62–72. <https://doi.org/10.1016/j.marchem.2011.12.004>.
- O'Connors, H. B., L. F. Small, and P. L. Donaghay. 1976. "Particle-Size Modification by Two Size Classes of the Estuarine Copepod *Acartia clausi*." *Limnology and Oceanography* 21: 300–308. <https://doi.org/10.4319/lo.1976.21.2.0300>.
- Oksanen, J., F. G. Blanchet, M. Friendly, et al., 2016. "vegan: Community Ecology Package."
- Peters, E., and D. N. Thomas. 1996. "Prolonged Darkness and Diatom Mortality I: Marine Antarctic Species." *Journal of Experimental Marine Biology and Ecology* 207: 25–41. [https://doi.org/10.1016/S0022-0981\(96\)02520-8](https://doi.org/10.1016/S0022-0981(96)02520-8).
- Picheral, M., S. Colin, and J.-O. Irisson. 2017. EcoTaxa, A Tool for the Taxonomic Classification of Images. <http://ecotaxa.obs-vlfr.fr>.
- Poulton, A. J., C. M. Moore, S. Seeyave, M. I. Lucas, S. Fielding, and P. Ward. 2007. "Phytoplankton Community Composition Around the Crozet Plateau, With Emphasis on Diatoms and *Phaeocystis*." *Deep Sea Research Part II: Topical Studies in Oceanography* 54: 2085–2105. <https://doi.org/10.1016/j.dsr2.2007.06.005>.
- R Core Team. 2023. "R: A Language and Environment for Statistical Computing." Vienna, Austria: R Foundation for Statistical Computing.
- Rembauville, M., I. Salter, N. Leblond, A. Gueneugues, and S. Blain. 2015. "Export Fluxes in a Naturally Iron-Fertilized Area of the Southern Ocean—Part 1: Seasonal Dynamics of Particulate Organic Carbon Export from a Moored Sediment Trap." *Biogeosciences* 12: 3153–3170. <https://doi.org/10.5194/bg-12-3153-2015>.
- Richman, S., and J. N. Rogers. 1969. "The Feeding of *Calanus Helgolandicus* on Synchronously Growing Populations of the Marine Diatom *Dirylum brighrwellii*." *Limnology and Oceanography* 14: 701–709. <https://doi.org/10.4319/lo.1969.14.5.0701>.
- Rigual-Hernández, A. S., T. W. Trull, S. G. Bray, I. Closset, and L. K. Armand. 2015. "Seasonal Dynamics in Diatom and Particulate Export Fluxes to the Deep Sea in the Australian Sector of the Southern Antarctic Zone." *Journal of Marine Systems* 142: 62–74. <https://doi.org/10.1016/j.jmarsys.2014.10.002>.

- Romanelli, E., J. Sweet, S. L. C. Giering, D. A. Siegel, and U. Passow. 2023. "The Importance of Transparent Exopolymer Particles Over Ballast in Determining Both Sinking and Suspension of Small Particles During Late Summer in the Northeast Pacific Ocean." *Elements of Science Anthropology* 11: 00122. <https://doi.org/10.1525/elementa.2022.00122>.
- Salter, I., A. E. S. Kemp, C. M. Moore, R. S. Lampitt, G. A. Wolff, and J. Holtvoeth. 2012. "Diatom Resting Spore Ecology Drives Enhanced Carbon Export From a Naturally Iron-Fertilized Bloom in the Southern Ocean." *Global Biogeochemical Cycles* 26: GB1014. <https://doi.org/10.1029/2010GB003977>.
- Salter, I., R. S. Lampitt, R. Sanders, et al. 2007. "Estimating Carbon, Silica and Diatom Export From a Naturally Fertilised Phytoplankton Bloom in the Southern Ocean Using PELAGRA: A Novel Drifting Sediment Trap." *Deep Sea Research Part II* 54: 2233–2259. <https://doi.org/10.1016/j.dsr2.2007.06.008>.
- Sanders, R. J., S. A. Henson, A. P. Martin, et al. 2016. "Controls Over Ocean Mesopelagic Interior Carbon Storage (COMICS): Fieldwork, Synthesis, and Modeling Efforts." *Frontiers in Marine Science* 3: 1–7. <https://doi.org/10.3389/fmars.2016.00136>.
- Schlitzer, R. 2002. "Carbon Export Fluxes in the Southern Ocean: Results From Inverse Modeling and Comparison With Satellite-Based Estimates." *Deep Sea Research Part II: Topical Studies in Oceanography* 49: 1623–1644. [https://doi.org/10.1016/S0967-0645\(02\)00004-8](https://doi.org/10.1016/S0967-0645(02)00004-8).
- Schuback, N., K. Oxborough, M. Burkitt-Gray, et al. 2024. "Phytoplankton Primary Productivity: A Dual-Incubation Approach for Direct Comparison of Photosystem II Photosynthetic Flux (JVPII) and ¹⁴C-Fixation Experiments." *Limnology and Oceanography: Methods* 22: 720–737. <https://doi.org/10.1002/lom3.10635>.
- Smetacek, V. 1999. "Diatoms and the Ocean Carbon Cycle." *Protist* 150: 25–32. [https://doi.org/10.1016/S1434-4610\(99\)70006-4](https://doi.org/10.1016/S1434-4610(99)70006-4).
- Smetacek, V., P. Assmy, and J. Henjes. 2004. "The Role of Grazing in Structuring Southern Ocean Pelagic Ecosystems and Biogeochemical Cycles." *Antarctic Science* 16: 541–558. <https://doi.org/10.1017/S0954102004002317>.
- Smyth, W. D., and J. N. Moum. 2019. "3D Turbulence." In *Encyclopedia of Ocean Sciences*, edited by J. K. Cochran, J. H. Bokuniewicz, and P. Yager, 486–496. London: Elsevier.
- Soppa, M. A., C. Völker, and A. Bracher. 2016. "Diatom Phenology in the Southern Ocean: Mean Patterns, Trends and the Role of Climate Oscillations." *Remote Sensing* 8, no. 5: 420. <https://doi.org/10.3390/rs8050420>.
- Steinberg, D. K., M. W. Silver, and C. H. Pilskaln. 1997. "Role of Mesopelagic Zooplankton in the Community Metabolism of Giant Larvacean House Detritus in Monterey Bay, California, USA." *Marine Ecology Progress Series* 147: 167–179. <https://doi.org/10.3354/meps147167>.
- Strzepek, R. F., M. T. Maldonado, K. A. Hunter, R. D. Frew, and P. W. Boyd. 2011. "Adaptive Strategies by Southern Ocean Phytoplankton to Lessen Iron Limitation: Uptake of Organically Complexed Iron and Reduced Cellular Iron Requirements." *Limnology and Oceanography* 56: 1983–2002. <https://doi.org/10.4319/lo.2011.56.6.1983>.
- Thevar, T., N. Burns, M. Ockwell, and J. Watson. 2023. "An Ultracompact Underwater Pulsed Digital Holographic Camera with Rapid Particle Image Extraction Suite." *IEEE Journal of Oceanic Engineering* 48: 566–576. <https://doi.org/10.1109/JOE.2022.3220880>.
- Thornton, D. C. O. 2002. "Diatom Aggregation in the Sea: Mechanisms and Ecological Implications." *European Journal of Phycology* 37: 149–161. <https://doi.org/10.1017/S0967026202003657>.
- Timmermans, K. R., and B. Van Der Wagt. 2010. "Variability in Cell Size, Nutrient Depletion, and Growth Rates of the Southern Ocean Diatom *Fragilariopsis kerguelensis* (Bacillariophyceae) After Prolonged Iron Limitation." *Journal of Phycology* 46: 497–506. <https://doi.org/10.1111/j.1529-8817.2010.00827.x>.
- Treguer, P., D. M. Nelson, A. J. Vanbennekom, D. J. Demaster, A. Leynaert, and B. Queguiner. 1995. "The Silica Balance in The World Ocean: A Reestimate." *Science* 268: 375–379. <https://doi.org/10.1126/science.268.5209.375>.
- Tréguer, P., C. Bowler, B. Moriceau, et al. 2018. "Influence of Diatom Diversity on the Ocean Biological Carbon Pump." *Nature Geoscience* 11: 27–37. <https://doi.org/10.1038/s41561-017-0028-x>.
- Twining, B. S., S. B. Baines, and N. S. Fisher. 2004. "Element Stoichiometries of Individual Plankton Cells Collected During the Southern Ocean Iron Experiment (SOFEX)." *Limnology and Oceanography* 49: 2115–2128. <https://doi.org/10.4319/lo.2004.49.6.2115>.
- Villareal, T. A., C. H. Pilskaln, J. P. Montoya, and M. Dennett. 2014. "Upward Nitrate Transport by Phytoplankton in Oceanic Waters: Balancing Nutrient Budgets in Oligotrophic Seas." *PeerJ* 2: e302. <https://doi.org/10.7717/peerj.302>.
- Ward, P., M. Whitehouse, R. Shreeve, et al. 2007. "Plankton Community Structure South and West of South Georgia (Southern Ocean): Links With Production and Physical Forcing." *Deep Sea Research Part I: Oceanographic Research Papers* 54: 1871–1889. <https://doi.org/10.1016/j.dsr.2007.08.008>.
- Williams, J. R., S. L. C. Giering, C. A. Baker, et al. 2024. "Inefficient Transfer of Diatoms Through the Subpolar Southern Ocean Twilight Zone." *Nature Geoscience* 18: 72–77. <https://doi.org/10.1038/s41561-024-01602-2>.
- Yamada, Y., Y. Tomaru, H. Fukuda, and T. Nagata. 2018. "Aggregate Formation During the Viral Lysis of a Marine Diatom." *Frontiers in Marine Science* 5: 167. <https://doi.org/10.3389/fmars.2018.00167>.

- Young, A. M., L. Karp-Boss, P. A. Jumars, and E. N. Landis. 2012. "Quantifying Diatom Aspirations: Mechanical Properties of Chain-Forming Species." *Limnology and Oceanography* 57: 1789–1801. <https://doi.org/10.4319/lo.2012.57.6.1789>.
- Zielinski, U., and R. Gersonde. 1997. "Diatom Distribution in Southern Ocean Surface Sediments (Atlantic Sector): Implications for Paleoenvironmental Reconstructions." *Palaeogeography Palaeoclimatology Palaeoecology* 129: 213–250. [https://doi.org/10.1016/S0031-0182\(96\)00130-7](https://doi.org/10.1016/S0031-0182(96)00130-7).

Supporting Information

Additional Supporting Information may be found in the online version of this article.

Submitted 09 August 2024

Revised 02 December 2024

Accepted 24 January 2025

SUPPORTING INFORMATION

Species-specific diatom dynamics shape their vertical distribution and export during bloom decline

Sarah L. C. Giering [1]*, Filipa Carvalho [1], Morten H. Iversen [2] [3], Zonghua Liu [1] [4], Océane Merchiers [5], C. Mark Moore [5], Michael Ockwell [6], Uta Passow [7], Alex J. Poulton [8], Elisa Romanelli [9], Thangavel Thevar [10], Richard Sanders [11] [12]

[1] National Oceanography Centre, Southampton, UK

[2] Alfred Wegener Institute Helmholtz-Center for Polar and Marine Research Bremerhaven, Bremerhaven, Germany

[3] MARUM and University of Bremen, Bremen, Germany

[4] School of Computing, Engineering and Technology, Robert Gordon University, Aberdeen AB10 7AQ, UK

[5] School of Ocean and Earth Science, National Oceanography Centre Southampton, University of Southampton, Southampton, SO14 3ZH, UK

[6] Hi-Z 3D LTD, 86-90 Paul Street, London, EC2A 4NE, UK

[7] Memorial University, St John's, Newfoundland and Labrador, Canada

[8] The Lyell Centre for Earth and Marine Sciences, Heriot-Watt University, Edinburgh, United Kingdom

[9] Earth Research Institute, University of California, Santa Barbara, CA, USA

[10] School of Engineering, University of Aberdeen, Aberdeen, United Kingdom

[11] Norwegian Research Centre, Jahnebakken 5, Bergen, Norway

[12] Bjerkenes Centre for Climate Research, Bergen, Norway

*Email: s.giering@noc.ac.uk (Corresponding author)

Running head

Diatom dynamics during bloom decline

Table of Contents

1. Figures

Figure S1. Vertical profiles of abundance and length of *F. kerguelensis* and *E. antarctica* during the four visits.

Figure S2. Comparison of chain length of *F. kerguelensis* and *E. antarctica* as imaged by LISST-Holo and FlowCam.

Figure S3. NMDS of particle composition throughout the water column during the study period.

Figure S4. Vertical profiles of Fv/Fm of samples collected from the MSC.

Figure S5. Vertical profiles of the contribution of *F. kerguelensis* and *E. antarctica* to total particle composition.

2. Supplementary Text

2.1 Analytical details for CTD casts

2.2 Hologram collection, extraction and sizing

2.3 Sinking material - Marine Snow Catcher and FlowCam

2.4 Fragmentation of particles during collection

3. Tables

3.1 Deployment details

3.2 Example images

4. References

1. Figures

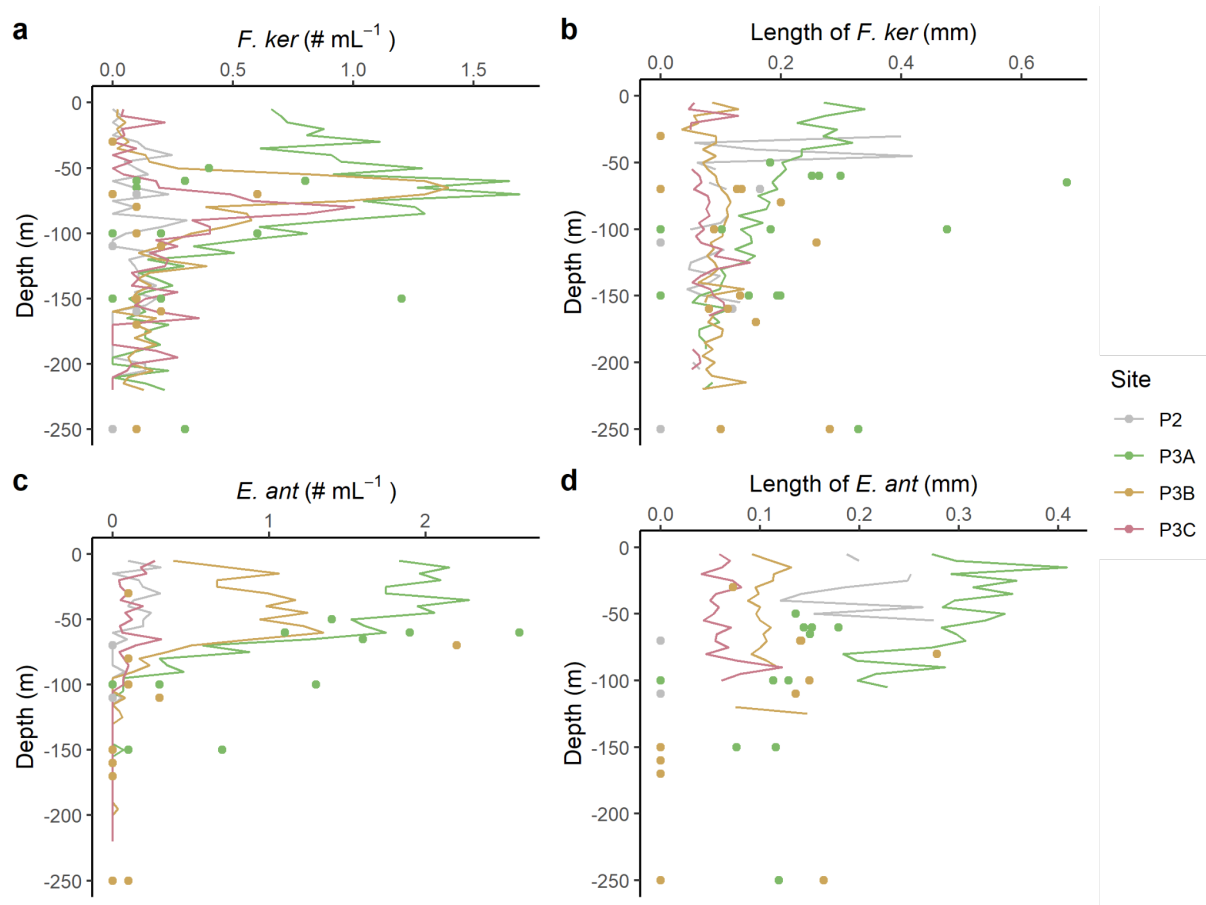


Figure S1 | Vertical profiles of abundance and length of *F. kerguelensis* and *E. antarctica* during the four visits. (a & c) Average abundance at each depth. (b & d) Average major axis length at each depth. Note change in x-axes. Lines show LISST-Holo-based estimates in 5-m bins. Dots show MSC-based estimates (T₀). Colours indicate visit: P2 in grey, P3A – P3C in green, orange and red, respectively.

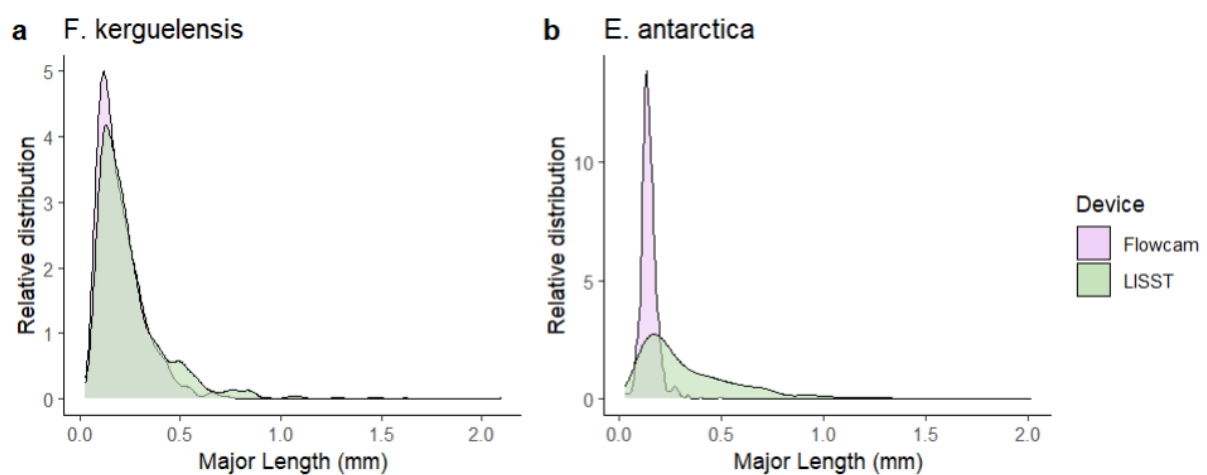


Figure S2 | Comparison of chain length of *F. kerguelensis* and *E. antarctica* as imaged by LISST-Holo and FlowCam. Data covers all images for (a) *F. kerguelensis* and (b) *E. antarctica* as imaged by FlowCam (purple) and LISST-Holo (green).

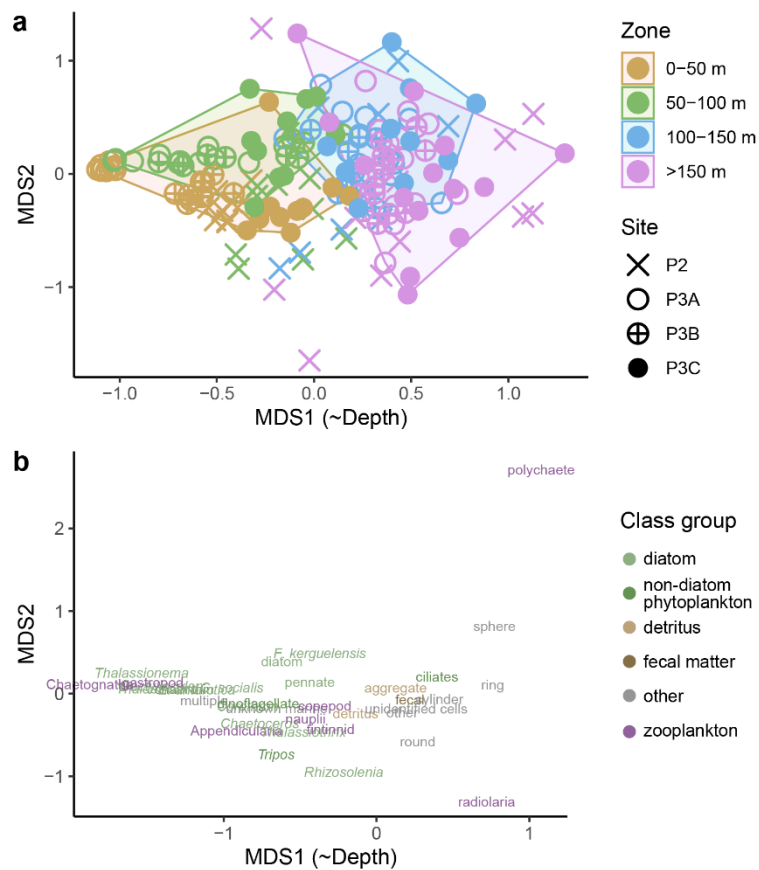


Figure S3| NMDS of particle composition throughout the water column during the study period. (a) NMDS analysis (stress = 0.22) shows a clear separation in particle composition between near-surface (0 - 100 m) and upper mesopelagic (100 - 250 m). Colours show depth zones and symbols show sites as indicated in the legend. Polygons show the extent of each depth zone for P3 (i.e. excluding P2). **(b)** Associated class scores show that phytoplankton drive near-surface communities, whereas detritus and other particles dominate upper mesopelagic particle composition. Colours indicate class group as shown in legend.

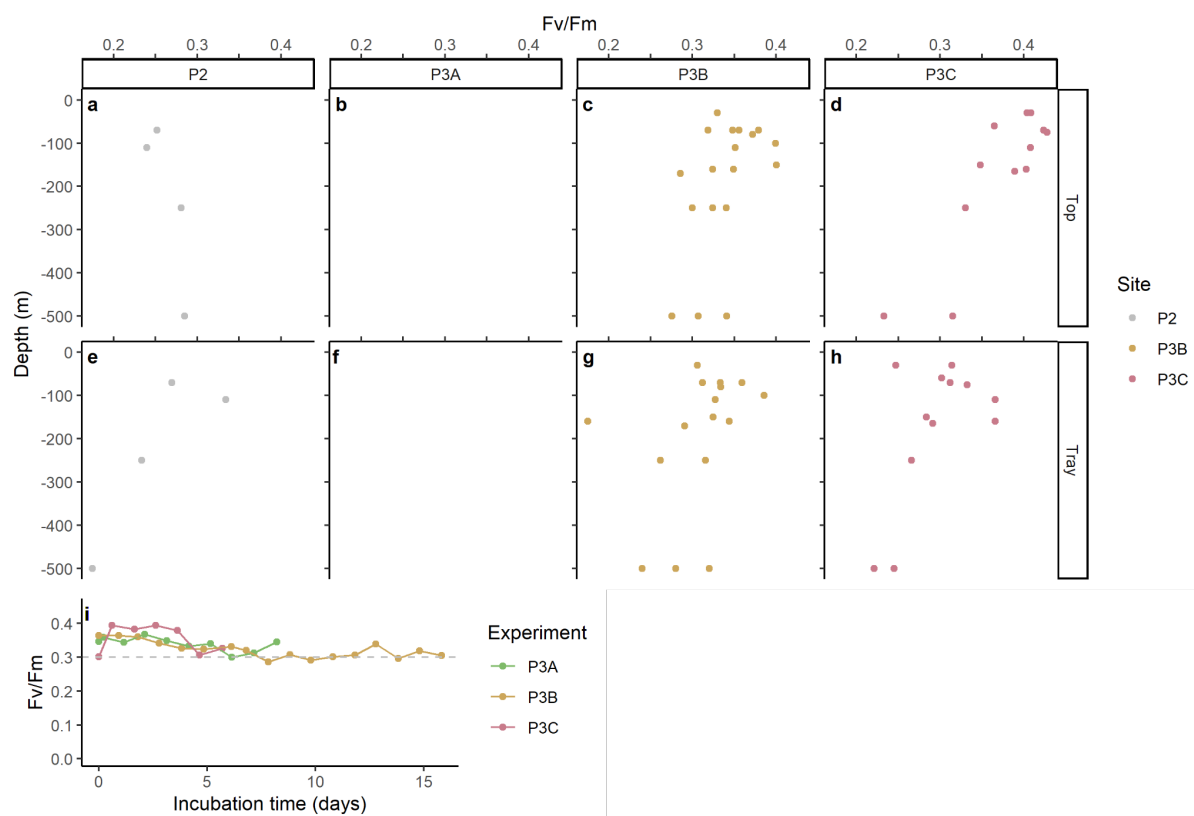


Figure S4| Vertical profiles of Fv/Fm of samples collected from the MSC (a-d) suspended fraction ('Top') and (e-h) fast-sinking fraction ('Tray') during (a, e) P2, (c, g) P3B and (d, h) P3C. Note, no data available for P3A (panel included for completeness). (i) Change over time of Fv/Fm of surface samples incubated in darkness. Three experiments were carried out, one each during P3A, P3B and P3C (green, yellow and red, respectively). Dashed grey line indicates a Fv/Fm of 0.3.

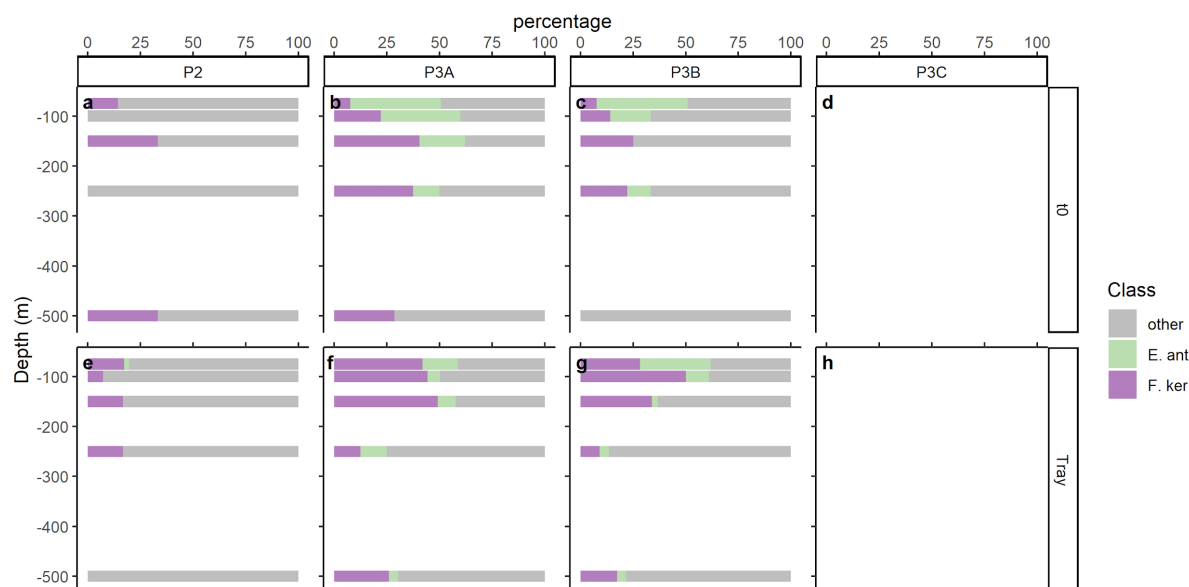


Figure S5 | Vertical profiles of the contribution of *F. kerguelensis* and *E. antarctica* to total particle composition (abundance in # mL⁻¹) in the MSC based on FlowCam images for the (a-d) suspended fraction ('T₀') and (e-h) fast-sinking fraction ('Tray') during (a, e) P2, (b, f) P3A and (c, g) P3B. Colours indicate *F. kerguelensis* (purple), *E. antarctica* (green) and other particles (grey). Note, no data available for P3C (panel included for completeness).

2. Text

2.1. Analytical details for CTD casts

The profiles were conducted pre-dawn to minimize the quenching effect, and chlorophyll fluorescence was calibrated using in situ chlorophyll samples from those casts (details below). After filtering out potentially quenched data, the calibration was applied to all fluorescence data, with no further quenching correction applied to the final results. Salinity was calibrated on board using water samples analysed on a Guildline Autosol 8400B salinometer. Water samples from discrete depths (15 mL) were analysed for nitrate, phosphate and silicate on board using a QuAAtro 39 segmented flow autoanalyser linked to a XY-2 Sampler (SEAL Analytical, UK). Water samples for chlorophyll-*a* (100-250 mL) were filtered onto GF/F filters (0.7- μm nominal pore size, 25-mm diameter, Whatman, UK), pigments extracted in 6 mL of 90% acetone for ~18-24 hours at 4°C in a fridge in the dark, and fluorescence measured on board using a Turner Designs Trilogy™ fluorometer set up with a non-acidification (after Welschmeyer, 1994, L&O 39) module and calibrated against pure chlorophyll-*a* extract (Sigma-Aldrich). Dissolved iron was measured as described by Ainsworth et al. (2023).

2.2. Hologram collection, extraction and sizing

A holographic image captures the interference pattern generated when a collimated light beam (658 nm solid-state diode laser) passes through a water sample with a 50 mm length. Objects within the water sample cause light to scatter, creating a distinctive interference pattern that is recorded in a 1600 × 1200 (W × H) image (hologram) with a pixel size of 4.4 μm . This pattern encodes information about the object's size and position, and objects can be reconstructed from it resulting in focussed monochrome images of the object.

The holograms were processed using FastScan (Thevar et al. 2023) including hologram reconstruction, particle autofocusing and extraction. As well as high-accuracy and robust particle extraction, this hologram processing suite was developed on an FPGA (Field Programmable Gate Array) to significantly accelerate hologram reconstruction and particle autofocusing. According to the recording parameters of LISST-Holo, FastScan reconstructed each full-size hologram in 100 planes within 50 mm recording length (two window planes were excluded to avoid noisy particles attached to the windows), extracted the focussed particles from the hologram, and output their vignettes. Particle size was extracted from these vignettes using the machine-learning-based method developed by Liu et al. (2023). Note that the volume for delicate particles with enclosed empty space may be overestimated, though these particles were rare.

Equivalent spherical diameter (ESD in mm) of a particle was calculated from the area (A in pixel) of the particle to calculate the diameter of a circle with the equivalent area, and then converted from pixel into mm assuming that there are 4.4 μm per pixel (p).

$$ESD = \sqrt{\frac{A}{\pi}} \times 2 \times \frac{p}{1000} \quad (\text{Eq. 1})$$

A particle's volume (V in mm^3) was then calculated as follows.

$$V = \frac{4}{3} \times \pi \times \left(\frac{ESD}{2}\right)^3 \quad (\text{Eq. 2})$$

Particle details calculated from the holograms were then summarised in 5-m depth bins. Bins were assigned based on rounded depth values, so that the 10-m bin covers images taken between 7.5 and 12.4 m depth. In order to calculate particle statistics, such as concentration, binned values (e.g. total particle number or volume) were divided by the summed volume of the LISST-Holo images taken at that depth interval, including empty holograms.

The size estimates based on the FastScan routine coupled with the structuredForest method seem generally good (Figure 4 by Liu et al. (2023)). The algorithm applies a hole filling operation. Consequently, for delicate structures with empty space, like *Thalassiosirix*, the algorithm assumes a solid structure. The volume estimate hence describes the volume encompassed by the particle rather than the volume of the particle (see Supporting Fig. S6 below). The interpretation of volume size spectra hence needs to be carefully considered. The calculation of number size spectra, especially when using MajAL (Takeuchi et al. 2019) should still be appropriate.

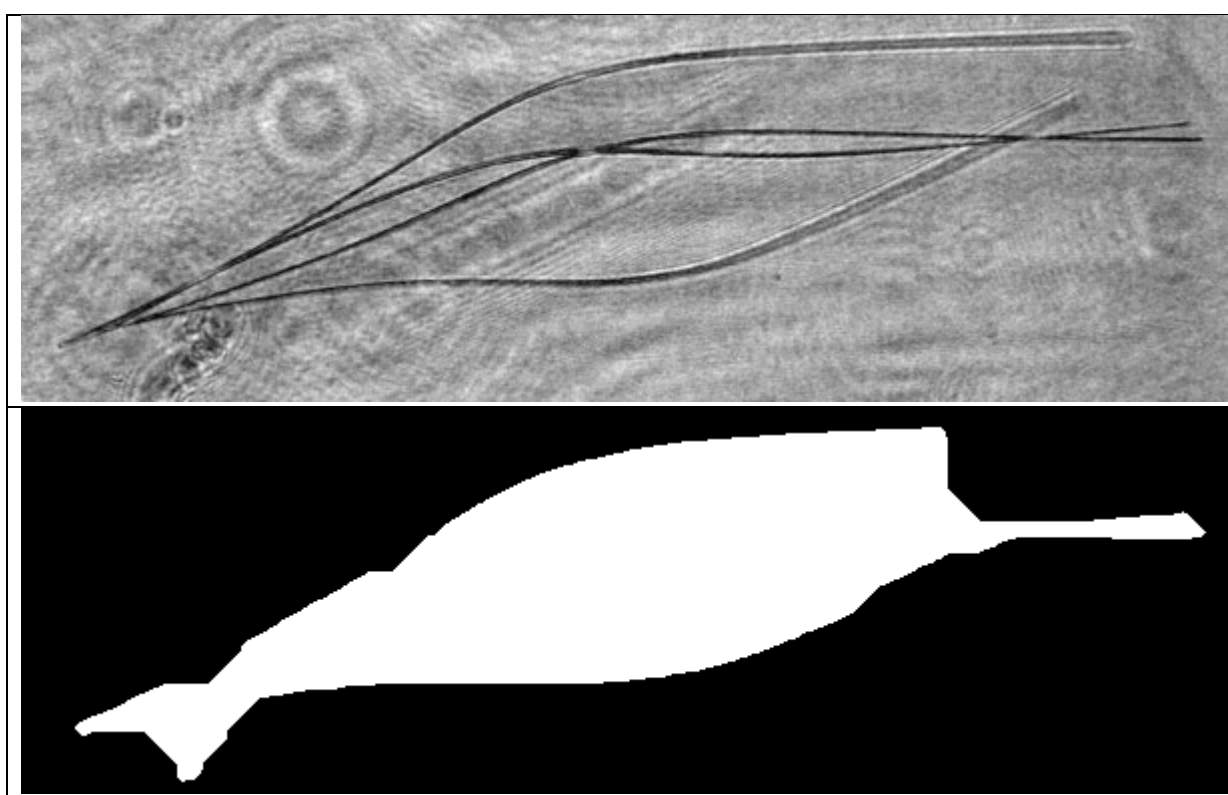


Figure S6. | Mask of *Thalassiothrix*, highlighting issues with the particle volume calculation. Top panel shows reconstructed image used for taxonomic classification, bottom panel shows mask used for volume and size calculations.

2.3. Sinking material - Marine Snow Catcher and FlowCam

The MSC is a large sampling bottle that is deployed open to a specific depth (here between 50 and 500 m depth). It holds 95 L of water and has a removable base section (8 L) fitted with a tray for collecting fast-sinking particles (18.5 cm diameter, 4 cm height, ~1 L volume). After recovery, a 5-L ‘time zero’ sample (T_0) was taken from the top section. The MSC was then left on deck for two hours to allow particles to settle. The top section (containing the suspended particles) was drained and removed to allow access to the base section, which contained the slow-sinking particles, and the tray, which contained the fast-sinking particles (FSP). Concentrations and fluxes of chlorophyll-a, biogenic silica, and particulate organic carbon for

each fraction are presented by Giering et al. (2023) and Williams et al. (2024). Here, we analysed the taxonomic microplankton community composition of the T₀ and Tray samples. For this, 50-200 mL of the sample were transferred into glass bottles, fixed with a final concentration of 3.6% formaldehyde (buffered with di-sodium tetraborate). Samples were stored in darkness in a cool place until onshore analysis. No formaldehyde samples were taken for P3C.

To identify and quantify particles collected by the MSC, we processed 10 mL of each formaldehyde-preserved sample using FlowCam 8410 (Yokogawa Fluid Imaging Technologies Inc.). Detailed methods are described by Romanelli et al. (2023). Briefly, particles in the samples are pumped through a glass cuvette past a microscopic camera, which takes colour images, at a magnification set to the 4x objective (capturing objects larger than 5 µm in diameter, though we identified only objects larger than approximately 80 µm in diameter as smaller particles could not be identified reliably). Imaged particles were counted and manually classified using the EcoTaxa platform (Picheral et al. 2017). The size and colour of particles was measured using Python. To do so, an image was converted to greyscale (where 0 means black and 255 means white), and the particle's mask was determined by applying a threshold value of 160. Some images contained smaller particles that were not of interest, and so we only retained the largest region of interest detected by the threshold. The mask's holes were filled and area, convex area, major length, mean grey value calculated. ESD and volume were calculated following Equations 1 and 2. Sizes were converted from pixel into mm assuming 1.4 µm per pixel.

The numerical concentration of sinking cells (C_{sink} in n mL⁻¹) and resulting fluxes (F in n cm⁻² d⁻¹) of *F. kerguelensis* and *E. antarctica* were calculated based on the equations by Giering et al. (2016, 2023) with slight modifications, considering number concentrations and using T₀ and Tray samples:

$$C_{\text{sink}} = (C_{\text{Tray}} - C_{\text{T0}}) \times V_{\text{Tray}} / (A_{\text{Tray}} \times h_{\text{MSC}}) \quad (\text{Eq. 3}),$$

$$F = C_{\text{sink}} \times V_{\text{MSC}} / (A_{\text{MSC}} \times t) \quad (\text{Eq. 4}),$$

where C_{Tray} and C_{T0} are respectively the concentrations (n mL⁻¹) in the tray and T₀ samples, V_{Tray} and V_{MSC} are respectively the volume of the tray section (~1000 mL) and the MSC (95 L), A_{Tray} and A_{MSC} are respectively the area of the tray (260 cm²) and the MSC (600 cm²), h_{MSC} is the height of the MSC (158 cm), and t the settling time (2 h). The percentage of sinking cells was calculated as the ratio between C_{sink} and C_{T0} .

2.4. Fragmentation of particles during collection

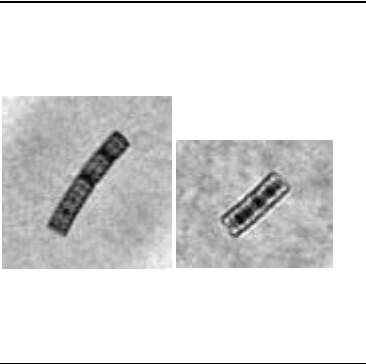
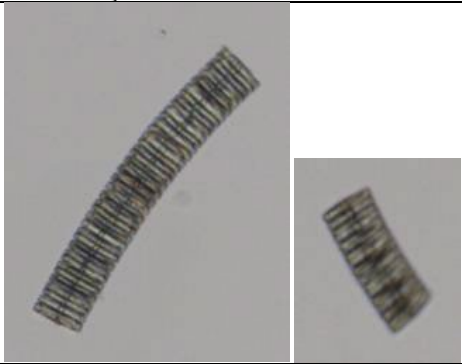
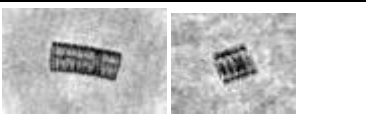
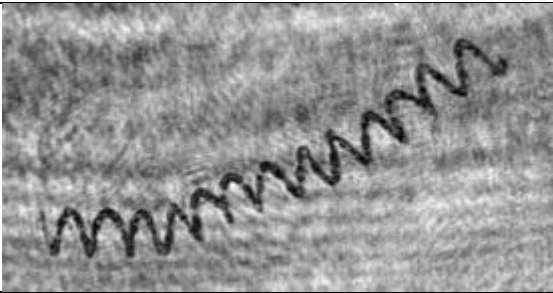
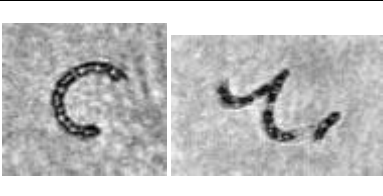
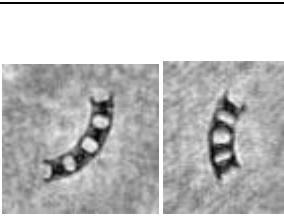
We did not find a systematic statistical difference in downcast vs upcast (t-test and paired t-test on 5-m binned data) in terms of total particle abundance, total particle volume, diatom abundance, or diatom volume. Out of the 11 profiles, we found significant differences for three profiles as follows. Profile 34 (paired t-test for total abundance with higher numbers during the downcast; $p = 0.01$, $n = 88$) was the profile with the highest number of diatoms and aggregates and had the most complex particle composition. Profile 205 (paired t-test for diatom volume with higher volume during upcast; $p = 0.04$, $n = 84$) and 313 (paired t-test for diatom volume with higher volume during downcast; $p = 0.02$, $n = 32$) were sampled during P3B and P3C, respectively, when diatom abundance was relatively low (Ainsworth et al. 2023). Owing to the lack of systematic response to the sampling direction in any of the particle characteristics, we included all profiles and combined downcast and upcast data when computing the depth profiles for further data analyses.

3. Tables

Table S1. | Deployment details for LISST-Holo and Marine Snow Catchers (MSC) during DY086.

Equipment	Cruise	Date	Time	Station	Latitude (N)	Longitude (E)	Cruise event number	Deployment number	Deployment depth (m)
LISST-Holo	DY086	2017-11-16	10:09	P3A	-52 41.40	-40 07.50	34	RCF001	226
LISST-Holo	DY086	2017-11-20	23:50	P3A	-52 46.52	-40 20.96	98	RCF005	228
LISST-Holo	DY086	2017-11-24	01:35	P2	-56 24.00	-41 13.00	120	RCF007	226
LISST-Holo	DY086	2017-11-25	16:15	P2	-56 38.00	-40 55.00	145	RCF009	225
LISST-Holo	DY086	2017-12-02	14:27	P3B	-52 41.74	-40 15.17	205	RCF013	227
LISST-Holo	DY086	2017-12-03	20:25	P3B	-52 31.00	-40 00.21	227	RCF014	226
LISST-Holo	DY086	2017-12-04	22:32	P3B	-52 43.24	-40 19.57	247	RCF017	226
LISST-Holo	DY086	2017-12-05	16:56	P3B	-52 43.30	-40 19.60	258	RCF018	228
LISST-Holo	DY086	2017-12-10	13:14	P3C	-52 41.70	-40 19.40	293	RCF021	226
LISST-Holo	DY086	2017-12-11	13:30	P3C	-52 43.00	-40 14.30	313	RCF023	226
LISST-Holo	DY086	2017-12-12	19:48	P3C	-52 38.80	-40 12.60	330	RCF025	224
MSC	DY086	2017-11-16	08:00	P3A	-52 41.42	-40 07.50	29	MSC006	60
MSC	DY086	2017-11-16	08:18	P3A	-52 41.42	-40 07.50	30	MSC007	100
MSC	DY086	2017-11-16	09:14	P3A	-52 41.42	-40 07.50	33	MSC010	150
MSC	DY086	2017-11-18	03:44	P3A	-52 41.82	-40 00.13	61	MSC015	60
MSC	DY086	2017-11-18	03:57	P3A	-52 41.86	-40 10.13	62	MSC016	150
MSC	DY086	2017-11-18	09:22	P3A	-52 41.86	-40 10.13	68	MSC019	100
MSC	DY086	2017-11-18	09:44	P3A	-52 41.86	-40 10.13	69	MSC020	500
MSC	DY086	2017-11-18	10:25	P3A	-52 44.99	-40 11.98	71	MSC022	250
MSC	DY086	2017-11-20	09:13	P3A	-52 44.99	-40 11.98	84	MSC027	65
MSC	DY086	2017-11-20	09:38	P3A	-52 46.52	-40 20.94	85	MSC028	60
MSC	DY086	2017-11-20	10:07	P3A	-52 45.09	-40 12.26	86	MSC029	500
MSC	DY086	2017-11-20	23:05	P3A	-52 45.09	-40 12.23	96	MSC034	150
MSC	DY086	2017-11-20	23:28	P3A	-52 45.09	-40 12.23	97	MSC035	100
MSC	DY086	2017-11-21	09:50	P3A	-52 45.09	-40 12.23	97	MSC036	150
MSC	DY086	2017-11-21	10:19	P3A	-56 24.07	-41 12.00	104	MSC037	500
MSC	DY086	2017-11-21	10:52	P3A	-52 39.31	-40 15.79	105	MSC038	50
MSC	DY086	2017-11-21	11:17	P3A	-52 39.31	-40 15.79	106	MSC039	100
MSC	DY086	2017-11-24	09:15	P2	-52 39.31	-40 15.79	130	MSC049	70
MSC	DY086	2017-11-25	07:28	P2	-52 42.53	-40 04.58	131	MSC050	110
MSC	DY086	2017-11-25	07:54	P2	-52 42.28	-40 06.13	132	MSC051	500
MSC	DY086	2017-11-25	08:24	P2	-52 42.28	-40 06.13	133	MSC052	250
MSC	DY086	2017-11-25	08:44	P2	-52 42.28	-40 06.13	134	MSC053	70
MSC	DY086	2017-11-25	13:02	P2	-52 42.40	-40 05.94	143	MSC060	160
MSC	DY086	2017-11-29	21:52	P3B	-52 42.32	-40 06.08	154	MSC061	250
MSC	DY086	2017-11-29	22:11	P3B	-52 42.32	-40 06.08	155	MSC062	160
MSC	DY086	2017-11-29	22:24	P3B	-52 42.32	-40 06.03	156	MSC063	70
MSC	DY086	2017-11-30	13:05	P3B	-52 41.74	-40 15.45	170	MSC067	110
MSC	DY086	2017-11-30	21:13	P3B	-52 41.74	-40 15.15	176	MSC068	70
MSC	DY086	2017-11-30	21:46	P3B	-52 41.25	-40 20.64	178	MSC070	500
MSC	DY086	2017-11-30	22:09	P3B	-52 43.25	-40 19.56	179	MSC071	250
MSC	DY086	2017-11-30	22:26	P3B	-52 41.86	-40 10.13	180	MSC072	70
MSC	DY086	2017-12-01	12:01	P3B	-52 44.99	-40 11.98	188	MSC076	110
MSC	DY086	2017-12-01	20:40	P3B	-52 46.52	-40 20.94	193	MSC077	500
MSC	DY086	2017-12-01	21:15	P3B	-56 38.00	-40 54.93	194	MSC078	150
MSC	DY086	2017-12-01	21:28	P3B	-56 38.00	-40 54.93	195	MSC079	100
MSC	DY086	2017-12-02	21:44	P3B	-56 38.01	-40 54.94	206	MSC081	250
MSC	DY086	2017-12-02	15:58	P3B	-56 38.01	-40 54.94	207	MSC082	160
MSC	DY086	2017-12-02	16:29	P3B	-56 38.00	-40 54.93	209	MSC084	70
MSC	DY086	2017-12-04	17:21	P3B	-52 42.28	-40 06.13	235	MSC092	30
MSC	DY086	2017-12-05	16:03	P3B	-52 41.74	-40 15.45	255	MSC099	500
MSC	DY086	2017-12-05	16:28	P3B	-52 43.25	-40 19.56	256	MSC100	170
MSC	DY086	2017-12-05	16:44	P3B	-52 43.25	-40 19.56	257	MSC101	80

Table S2 | Example images for *F. kerguelensis* and *E. antarctica* from LISST-Holo and MSC + FlowCam. For each species, different orientations and sizes are shown. Similar-looking examples are selected for each instrument. Images for MSC + FlowCam are scaled to 70% for layout purposes. A scale bar, applicable to all images, is provided in the first row of each column.

Sp.	LISST-Holo	MSC + FlowCam
<i>F. kerguelensis</i>		
		
		
<i>E. antarctica</i>		
		
		

4. References

- Ainsworth, J., A. J. Poulton, M. C. Lohan, M. C. Stinchcombe, A. J. M. Lough, and C. M. Moore. 2023. Iron cycling during the decline of a South Georgia diatom bloom. *Deep Sea Res. Part II Top. Stud. Oceanogr.* **208**: 105269. doi:10.1016/j.dsr2.2023.105269
- Giering, S. L. C. and others. 2023. Vertical imbalance in organic carbon budgets is indicative of a missing vertical transfer during a phytoplankton bloom near South Georgia (COMICS). *Deep Sea Res. Part II Top. Stud. Oceanogr.* **209**: 105277. doi:10.1016/j.dsr2.2023.105277
- Giering, S. L. C., R. Sanders, A. P. Martin, C. Lindemann, K. O. Möller, C. J. Daniels, D. J. Mayor, and M. A. St. John. 2016. High export via small particles before the onset of the North Atlantic spring bloom. *J. Geophys. Res. Oceans* **121**: 6929–6945. doi:10.1002/2016JC012048
- Liu, Z., S. Giering, T. Thevar, N. Burns, M. Ockwell, and J. Watson. 2023. Machine-Learning-based Size Estimation of Marine Particles in Holograms Recorded by a Submersible Digital Holographic Camera. *OCEANS 2023 - Limerick*. Proceedings of the OCEANS 2023 - Limerick. 1–8.
- Picheral, M., S. Colin, and J.-O. Irisson. 2017. EcoTaxa, a tool for the taxonomic classification of images. <http://ecotaxa.obs-vlfr.fr>.
- Romanelli, E., J. Sweet, S. L. C. Giering, D. A. Siegel, and U. Passow. 2023. The importance of transparent exopolymer particles over ballast in determining both sinking and suspension of small particles during late summer in the Northeast Pacific Ocean. *Elem. Sci. Anthr.* **11**: 00122. doi:10.1525/elementa.2022.00122
- Takeuchi, M., M. J. Doubell, G. A. Jackson, M. Yukawa, Y. Sagara, and H. Yamazaki. 2019. Turbulence mediates marine aggregate formation and destruction in the upper ocean. *Sci. Rep.* **9**: 16280. doi:10.1038/s41598-019-52470-5
- Thevar, T., N. Burns, M. Ockwell, and J. Watson. 2023. An Ultracompact Underwater Pulsed Digital Holographic Camera With Rapid Particle Image Extraction Suite. *IEEE J. Ocean. Eng.* **48**: 566–576. doi:10.1109/JOE.2022.3220880
- Williams, J. R. and others. 2024. Inefficient transfer of diatoms through the subpolar Southern Ocean twilight zone. *Nat. Geosci.* 1–6. doi:10.1038/s41561-024-01602-2